Master's thesis

NTNU
Norwegian University of Science and Technology
Faculty of Engineering
Department of Marine Technology

Sondre Fagerbakke

Numerical and Experimental Investigation of a Floating Substation

Master's thesis in Marine Technology
Supervisor: Trygve Kristiansen
June 2023

NTNU
Norwegian University of
Science and Technology

Sondre Fagerbakke

Numerical and Experimental Investigation of a Floating Substation

Master's thesis in Marine Technology
Supervisor: Trygve Kristiansen
June 2023

Norwegian University of Science and Technology
Faculty of Engineering
Department of Marine Technology

NTNU
Norwegian University of
Science and Technology

Preface

This thesis is the final contribution to my Master of Science degree within Marine Technology, specializing in hydrodynamics at the Department of Marine Technology, Norwegian University of Science and Technology in Trondheim, Norway. The thesis has been carried out in the spring of 2023, with a workload corresponding to 30 ECTS.

During autumn 2022, the concept was investigated as a part of the project thesis, and the work have been continued in this thesis. Which includes the short literature review, introduction, theory and the numerical study.

The studies consists of numerical simulations and experimental test of the floating substation concept provided by Sevan SSP.

Sondre Fagerbakke

Trondheim, 9th June 2023

Acknowledgment

This thesis have been carried out under the supervision from Professor Trygve Kristiansen at the Department of Marine Technology, NTNU. His knowledge about hydrodynamics, guidance and ability to pass on his knowledge have been highly appreciated.

I would also like to give appreciation to the lab technicians, Trond Innset, Robert Opland and Terje Rosten. Thanks to them there was a model to use in the experiments, and their support throughout the experiments was very helpful. They was a pleasure to work with.

Finally I want to thank me. I want to thank me for believing in me. I want to thank me for doing all this hard work. I want to thank me for having no days off. I want to thank me for never quitting. I want to thank me for being me at all time during this masters.

Abstract

The floating substation concept design developed by Sevan SSP has the potential to be used in different industries, ranging from offshore wind, carbon capture storage to offshore aquaculture farming. The special part about the design is the low freeboard, which makes it more prone to wave overtopping and deck flooding. The non-linear effects and the implications was supposed to be the topic of the thesis, however wave overtopping occurred less frequently than assumed. Which led to a change in area of focus in the thesis to the general stability of the structure.

The concept was investigated through numerical analyses and a model experiment in the Small Towing Tank at NTNU. The numerical analyses were performed using WAMIT. By examining different bilge keel diameters, draught, pre-tension of mooring and I55 values the results showed that the model was mostly sensitive to changes in the bilge keel diameter. The analyses were performed in order to replicate the model experiments.

There was a total of six different configurations tested during the model experiments. Two configurations with different bilge keel diameter, two configurations at a different draughts and two configurations with different pre-tension of the mooring.

The results from the experiments were compared to the numerical results in both surge, heave and pitch, coinciding well. Findings from the experiments shows that there are tendencies to Mathieu Instability for the configurations with a large bilge keel, as resonance in pitch occurs at the same period there are non linear movements in roll. The configurations with a smaller bilge keel do not experience non linear movements in roll to such a large extent.

Sammendrag

Konseptet "Floating Substation" er utviklet av Sevan SSP og har potensial til å bli brukt i flere ulike bransjer, fra offshore vindkraft, karbonfangst og -lagring til offshore akvakultur. Det spesielle med designet er den lave fribordshøyden, noe som gjør strukturen mer utsatt for bølgetopping og oversvømmelse på dekk. De ikke-lineære effektene og konsekvensene av dette skulle være hoved temaet for avhandlingen, men bølgetoppingen forekom mindre hyppig enn antatt. Dette førte til en endring i fokuset i oppgaven, til et fokus på den generelle stabiliteten til strukturen.

Konseptet ble undersøkt gjennom numeriske analyser og modellforsøk i den lille slepetanken på NTNU. De numeriske analysene ble utført ved hjelp av WAMIT. Ved å undersøke ulike diametere på skjørtet, dypgang, forspenning av forankring og I55 viste resultatene at strukturen var mest sensitiv for endringer i diameteren på skjørtet. Analysene ble utført for å replikere modellforsøkene.

Det ble totalt testet seks ulike konfigurasjoner under modellforsøkene. To konfigurasjoner med ulik skjørt diameter, to konfigurasjoner med forskjellig dypgang og to konfigurasjoner med forskjellig forspenning av forankringen.

Resultatene fra forsøkene ble sammenlignet med de numeriske resultatene i både jag, hiv og stamp. Hvor de samsvarte godt. Funnene fra forsøkene viser at det er tendenser til Mathieu-instabilitet for konfigurasjoner med store skjørt, da resonans i stamping oppstår samtidig som det forekommer ikke linære bevegelser i rull. Dette opptrer ikke i like stor grad for konfigurasjoner med mindre skjørt.

Table of Contents

Chapter 1

1 Introduction

Sevan SSP's concept design with the floating substation design can be used within in a variety of industries where the onboard processes doesn't require people to be present, except for maintenance or repairs. This enables the possibilities to reduce the cost of the operations, but also building costs as it allows for an interesting design where the floater will be exposed to wave topping. Which is due to a relatively low freeboard on the substation. During wave topping, the whole unit will be submerged or partially submerged under water.

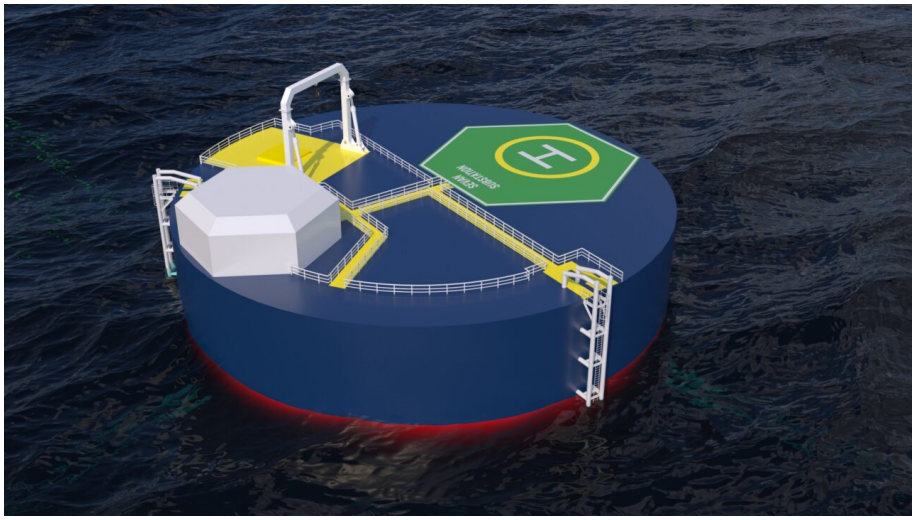

Figure 1: The floating substation concept illustrated by Sevan SSP [10]

The main proposal for the design is to use it as a power conversion and distributor for offshore windfarms. The substation may also be used as a feed tank in the aquaculture industry for offshore located cages. It is also possible to use the same design, for other purposes like carbon capture and storage injection. Such as in the Stella Maris project, where this substation is proposed to use if the project is realised [11]. With an estimated increase in floating floating offshore wind from 10 GW to 250 GW in 2050, there is a huge potential market for this substation [6]. Within the aquaculture industry there is also a great potential for this substation to function as a feeding tank. The industry has set a goal of growing five times by 2050, where most of this growth will happen at exposed locations [2].

Wave overtopping has the possibility to lead to interesting movements, especially in combination Mathieu instability. As the GM is quasi-static in waves, the substation may start to roll when it is pitch excited, due to being static unstable. The wave overtopping is also of interest, as the green sea have the possibility to damage structures on deck.

With an estimated free board of 11 meters for the unit, the wave overtopping is assumed to occur for moderate to large wave heights.

1.1 Short Literature Review

Wave overtopping has been a reasearch topic for several types of marine structures, where the research has been performed by numerical simulations and model tests. Most of the research regarding green sea wave overtopping has been regarding structures mounted at the sea bottom, or for floating production, storage and offloading (FPSO) structures that are shaped like a ship. Which makes the studies of less interest. However there have been performed studies on breakwaters, both floating and bottom-fixed. Results from research on breakwaters with rectangular shape shows that wave overtopping occurs when the freeboard/ incident-wave ≤ 0.78, combined with smaller waves being transmitted from the structure. [8]. Another relevant structure is a heave buoy type of Wave Energy Convector (WEC), which D.Short wrote a master thesis about. Which is relatively similar to the design of the unmanned floating structure. Where the results indicate that overtopping damps the amplitude motions experienced at frequencies close to resonance. [12] The same conclusions were found in another study of floating breakwaters performed by K.L. Jeong and Y.G.Lee [7]. Where the research indicated that the model with the lowest freeboard had the lowest responses.

1.2 Scope of Work

During the project thesis, the main goal of this master thesis was to examine how wave over topping affected the rigid body motions in surge, heave, roll and pitch. Which during the experimental tests proved to occur in less sea states than anticipated. This resulted in a change of the focus for the thesis, where the new area of focus was the general stability of the structure.

The objectives and scope of work in this thesis have been:

1. Generate a better understanding of wave overtopping and the Mathieu instability phenomenon.
2. Perform numeric analyses in WAMIT to compute the rigid body motions.
3. Preparation of execution of experimental tests.
4. Process experimental results to obtain RAOs of rigid body motions.
5. Discuss the effects of the different bilge keel, draughts and pre tension of the mooring.

1.3 Structure of the thesis

Chapter 2 describes the relevant theory behind the methods and results presented in the thesis. While Chapter 3 present the Floating Substation, with dimensions and mass properties combined with figures of the model. In Chapter 4 there is an overview of WAMIT and the usage in the thesis. It also includes the panel model,

mesh refinement study and a overview of the different configurations. Chapter 5 describes the experiments performed in the Small Towing Tank at Tyholt, Trondheim. The model, setup, instrumentation, error sources and precision are also mentioned. Chapter 6 present the results from the parameter study, where different bilge keel models, draughts, pre-tension on mooring and different values of I55 are examined numerically and discussed. The experimental results are presented in Chapter 7, where they are also discussed. Chapter 8 presents the conclusion and further work.

Chapter 2

2 Theory

Within this chapter relevant theory regarding the methods behind the master thesis will be outlined.

2.1 Potential Flow Theory

The potential flow theory can be used to describe the interaction between bodies and surface waves. In order to use this theory, three assumptions must be made. It is assumed that the flow is inviscid, irrotational and incompressible. By fullfilling those assumptions, the flow is ideal. In a 2D Cartesian coordinate system, the fluid velocity can be written as functions of the derivatives of the velocity potential in each direction [1].

$$V = \nabla\phi = i\frac{\partial\phi}{\partial x} + k\frac{\partial\phi}{\partial z} \tag{1}$$

For the assumption regarding the irrotational flow, the vorticity vector $\nabla \times V = 0$ in the fluid. The assumption about the incompressible fluid shows that $\nabla \cdot V = 0$. Which indicates that the fluid satisfies the Laplace equation below.

$$\Delta^2\phi = \frac{\partial^2\phi}{\partial x^2} + \frac{\partial^2\phi}{\partial z^2} = 0 \tag{2}$$

The Laplace equation must be solved along with three boundary value problems. The first problem is stated in Equation 3 which says that there is no flow through the sea bed.

$$\left.\frac{\partial\phi}{\partial z}\right|_{z=-h} = 0 \tag{3}$$

Equation 4 contains the non-linear dynamic free surface boundary condition. This requirement stipulates that the fluid pressure at the free surface must be equal to the surrounding pressure.

$$\frac{\partial\phi}{\partial\phi} + \underbrace{\frac{1}{2}\left[\left(\frac{\partial\phi}{\partial x}\right)^2 + \left(\frac{\partial\phi}{\partial z}\right)^2\right]}_{\text{non-linear}} + g\zeta = 0 \quad \text{at z}\zeta \tag{4}$$

Finally, the non-linear kinematic free surface boundary condition in Equation 5 requires that fluid particles on the free surface move at the same speed as the free surface, ensuring that they remain on the free surface.

$$\frac{\partial \zeta}{\partial t} = \frac{\partial \phi}{\partial z} - \underbrace{\frac{\partial \phi}{\partial x}\frac{\partial \zeta}{\partial x}}_{\text{non-linear}} \quad \text{at z} = \zeta \tag{5}$$

The velocity potential ϕ must satisfy Equation 2 and the three boundary conditions in Equation 3, Equation 4 and Equation 5. When solving the velocity potential for higher orders it is assumed that the surface potential ϕ and surface elevation ζ must be expressed as a pertubation series shown in Equation 6 and Equation 7 where $\epsilon = k\zeta$. It is possible to directly substitute the perturbation series into the continuity equation and first boundary condition. However for the second and third boundary value problems, the location of the free surface boundary condition must be known. The free surface is unknown, and must therefore be approximated by a Taylor expansion about z=0.

$$\phi = \epsilon\phi_1 + \epsilon^2\phi_2 + .. \tag{6}$$

$$\eta = \epsilon\eta_1 + \epsilon^2\eta_2 \tag{7}$$

2.1.1 Linear Wave Theory

Regular waves possess an amplitude, period and wave length. The waves are usually characterised by the wave period and wave steepness, $\epsilon = H/\lambda$. Where H is the wave height. Further on the ratio between the water depth, h, and wavelength, λ affects the formulas. The water depth is seen as finite water when $h/\lambda \leq 0.5$. For higher values, the water is defined as deep water. h is the water depth and λ is the wavelength [1].

2.2 Radiation and Diffraction

Analysing the motions of a structure includes a solution for the radiation and diffraction problem. This will be done using WAMIT in the project thesis.

Deep water, regular incident waves, steady-state condition and zero forward speed is presumptions made along with the linear potential flow theory. By assuming linearity and steady-state condition the superposition principle becomes valid, and the velocity potential can then be decomposed into eight problems. One for each degree of freedom, one for the undistributed incoming wave, and one for the diffracted wave. These problems may be solved separately, and the solution will be the total of all the solutions. The diffraction problem can be written as in Equation 8 where ϕ_0 is the velocity potential of the undisturbed wave, also called "Froude Krylov", and ϕ_7 is the diffraction term. This term must be satisfied at the body surface, S_{0B}, to satisfy the impermeability condition in Equation 9.

$$\phi_{diff.} = \phi_0 + \phi_7 \tag{8}$$

$$\frac{\partial(\phi_0 + \phi_7)}{\partial n} \Big| S_{0,B} = 0 \tag{9}$$

Within the radiation problem, the body is forced to oscillate in the six degrees of freedom. Seen from Equation 10. When the body oscillates it is created waves, whose creates hydrodynamic and hydrostatic loads on the structure. The hydrodynamic loads causes added mass and damping, and is frequency dependent. While the restoring force is not frequency dependent, and comes from the hydrostatic loads due to change of buoancy in the forced body motions. This radiation problem must also satisfy the impermeability condition on the body surface as in Equation 11. As the structure investigated will be moored during the experiments, additional mooring line restoring must be included in the numerical analysis to get the same responses.

$$\phi_{rad.} = \sum_{j=1}^{6} \phi_j \tag{10}$$

$$\frac{\partial \phi_j}{\partial n} \Big| S_{O,B} = n_j \quad j = 1..6 \tag{11}$$

The total diffraction problem can be written as the sum of the diffraction problem and radiation problem seen in Equation 12.

$$\phi = \phi_{diff} + \phi_{rad} \tag{12}$$

2.3 Added Mass and Damping

2.3.1 Added Mass

Added mass refers to a phenomenon that occurs when a body moves in fluids. In high density fluid, such as water, the added mass are important to account for. Added mass is caused by acceleration of fluid particles near the moving body. The particles accelerate because they are pushed by the body. The added mass coefficient is used to quantify the added mass effect. It is defined as the ratio of the added mass to the mass of the structure. The coefficient is a function of the structure's shape, size, as well as frequency. As it is frequency dependent. Where a negative coefficient means that it is out of phase with the motion of the body.

2.3.2 Damping

For a body in a fluid moving at the resonance frequency, the limiting factor is the damping response. There are two types of damping that are relevant, and those are viscous damping and wave radiation. Using linear potential flow theory, the viscous effects are not accounted for as the fluid is assumed irrotational. As long as the viscous loads are small compared to potential flow theory they can be neglected. When the loads becomes significant, as they does for larger movements of the body, this affects the added mass, damping and excitation loads. Which is the case for this floating unit.

Viscous damping is separated into friction and flow separation, where the last mentioned is the main source of damping. Accounting for this in a 3D model is yet to be found. However for a 2D model, one option is to include the Morison drag load term as in

$$F_D = 0.5\rho C_D D u_r |u_r| \tag{13}$$

C_D is the drag coefficient, D is the diameter and u_r is the relative velocity for a 2D circular cylinder. For a cylinder structure with skirt, the values needed to be used are unknown. One option is approximating loads around the circumference by using Morison types of loads to simulate the quadratic damping, added mass and excitation loads.

The flow velocity u_r is affected by the relative motion of the body, the velocity of coupled body motions and incident waves. With coupling in heave and pitch, the relative motion will be a result of incident wave particle velocity, heave velocity and coupled pitch velocity. The velocity is measured at the tip of the skirt, subtracted the velocities of the body motions. Resulting in equation Equation 14.

$$u_r = u_w - \dot{\eta}_3 + \dot{\eta} b \tag{14}$$

Where b is the the distance load is used over. Equation 14 inserted into Equation 13 gives the equation Equation 15.

$$F_D = 0.5\rho C_D D(u_w - \dot{\eta}_3 + \dot{\eta} b)|(u_w - \dot{\eta}_3 + \dot{\eta} b)| \tag{15}$$

For the floating unit, with the skirt, the viscous damping will be significant. It is possible to divide the damping term into two terms, where one is linear and the other is quadratic. Where the quadratic damping term can reduce the over predictions of the potential flow. The equation of motion can written as in :

$$\sum_{j=1}^{6}[(M_{kj} + A_{kj}\ddot{\eta}_j) + B_{kj}^{(1)}\dot{\eta}_j + B_{kj}^{(2)}\dot{\eta}_j|\dot{\eta}_j| + C_{kj}\eta] = F_j e^{i\omega t} \tag{16}$$

The quadratic damping term $B_{kj}^{(2)}$ can be found through CFD analysis or linearisation of the two damping terms. Expressed as one term $B_{kj}^{(eqv.)}$.

$$B_{kj}^{(eqv.)} = b_1 + b_2|\dot{\eta}| \tag{17}$$

2.4 Rigid Body Motions

A rigid body in waves and and currents moves in six degrees of freedom (DOF), with a set of points on the body that does not move relative to each other. The DOF's consists of three translational modes and three rotational modes. The name of the translational modes are surge, sway, heave, and the names of the rotational modes are roll, pitch and yaw. They are denoted in the order of η_i where i = 1,2,..6. Illustrated below in Figure 2, in a Cartesian coordinate system. For this project thesis the motions in surge, heave, roll and pitch will be of interest.

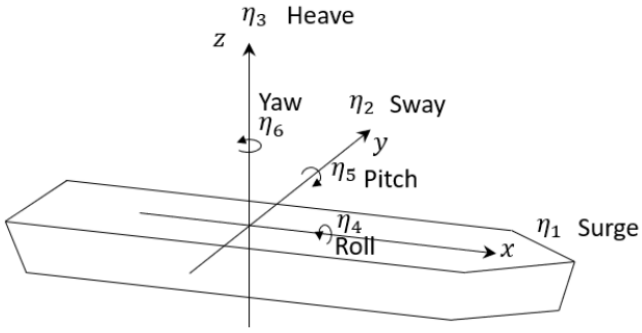

Figure 2: Six degrees of freedom rigid body motions, η_i , i = 1,..,6

Further on the rigid body motions can be written as equation [4]:

$$\sum_{k=1}^{6}[(M_{jk} + A_{jk})\ddot{\eta}_k + B_{jk}\dot{\eta}_k + C_{jk}\eta_k] = F_j, \quad j = 1, .., 6 \tag{18}$$

$M_{jk}, A_{jk}, B_{jk}, C_{jk}$ are the mass, added mass, damping and restoring mode in j due to motion in mode k. While F_j is the excitation force.

For harmonic motions of the floating unit, the undamped resonance period can be written as:

$$T_{n,j} = 2\pi\sqrt{\frac{M_{jj} + A_{jj}}{C_{jj}}} \tag{19}$$

The body motions are given a Response Amplitude Operator(RAO) and is denoted

to $H(\omega)$, which is the ratio between the body motion and the incident wave amplitude, ζ_a.

$$H_j(\omega) = \frac{\eta_{ja}}{\zeta_a} \tag{20}$$

The linear RAO can be estimated as in [1]:

$$\frac{\eta_{3a}}{\zeta_a} = \frac{f_{3a}}{-\omega^2(M + A_{33}) + i\omega B_{33} + C_{33}} \tag{21}$$

ω is the angular frequency of the wave, while f_{3a} is the heave excitation amplitude and i is the imaginary unit.

2.5 Mathieu instability

Mathieu instability occurs due to high variation of GM in waves, and arises from the coupling between heave and roll motion. However, for our circular floater, this also applies for heave-pitch movements. The effect is associated with the presence of bilge keels and fluid viscosity in the area of the resonant condition. As the coupling between heave and roll/pitch nonlinear, it is largely affected by large amplitude motion. Liao and Yeung [9]

The instability is related to the geometrical properties of the floating unit, the location of center of gravity and the amplitude of the heave motion. It is most likely that the instability will occur at the heave resonance frequency when heave amplitude is sufficiently large.

There is some coupling in roll motion due to pitch, but usually heave is the dominant factor. The roll equation can written as in Equation 22:

$$(I_{44} + A_{44})\frac{d^2\eta_4}{dt^2} + B_{44}\frac{d\eta_4}{dt} + \rho g \nabla(\overline{GM}_M + \delta\overline{GM} sin(\omega_e t + \beta))\eta_4 = 0 \tag{22}$$

Where heave, pitch and wave motions are represented by the term:

$$\rho g \nabla \delta\overline{GM} sin(\omega_e t + \beta))\eta_4 \tag{23}$$

Equation 22 is an approximation due to that the coupling from sway and yaw have been neglected, and the damping has been linearized. With waves coming in from head, the roll excitation moment from waves is zero. [3] However rolling can be experienced due to instabilities. When there is a small perturbation from equilibrium, the motions will increase with time.

Equation 22 may also be written as:

$$\frac{d^2\eta_4}{dt^2} + 2\zeta\omega_n\frac{d\eta_4}{dt} + \omega_n^2\left(1 + \frac{\rho\overline{GM}}{\overline{GM}_M}sin(\omega_e t + \beta)\right)\eta_4 = 0 \tag{24}$$

Where the natural roll frequency is ω_n.

$$\omega_n = \sqrt{\frac{\rho g \nabla \overline{GM_M}}{I_{44} + A_{44}}} \tag{25}$$

The damping ratio ζ is the ratio between damping and the critical damping.

$$\zeta = \frac{B_{44}}{2\sqrt{(I_{44} + A_{44}\rho g \nabla \overline{GM_M}}} \tag{26}$$

From the given equations is is observable that the stability of structures depends on ω_n/ω_e, $\rho\overline{GM}/\overline{GM}$ and ζ. Where ω_e is the frequency of the encountering waves.

Figure 3 shows the stability diagram for the Mathieu equation for ship rolling, in regards of of $\rho\overline{GM}/\overline{GM}$ and ω_n/ω_e. Where the unshaded areas shows instability domains. The dangerous combination are in the vicinity of $\omega_n/\omega_e = 0.5$, 1, 1.5 and higher, when $\rho\overline{GM}/\overline{GM}$ is small. It is observable that higher damping requires higher $\rho\overline{GM}/\overline{GM}$ for the instability to occur. The shaded areas shows domains where the ratio between roll damping and critical damping is zero.

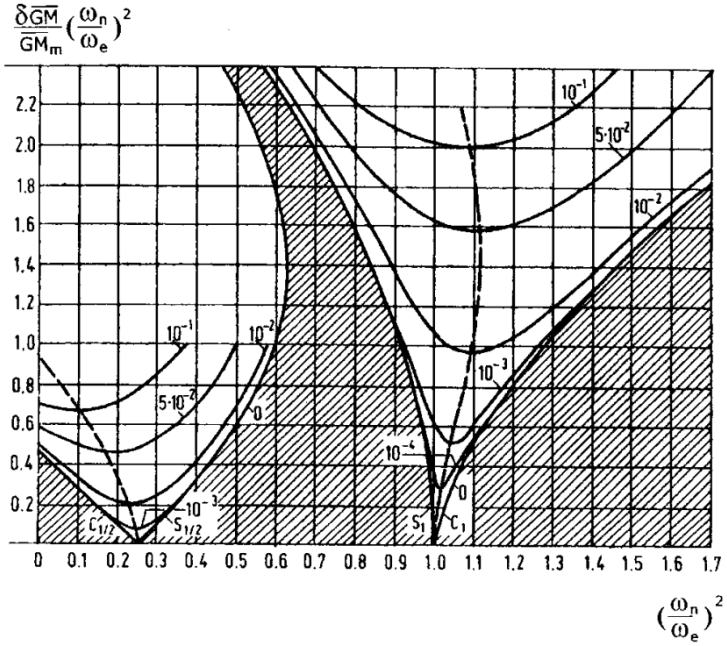

Figure 3: Stability diagram of Mathieu Instability

2.6 Froude Scaling

The Froude number is a dimensionless number defined as the relationship between inertia and gravity forces, and ensures that the gravity forces are correctly scaled. The equation is written as in Equation 27. It is possible to maintain similarities between the forces and dimensions in full- and model scale, when the Froude number is the same for both of them.

$$Fr = \frac{u}{\sqrt{gL}} \tag{27}$$

The scaled model will have the same geometry as the full size model, with the dimensions being linearly scaled. Further on the quantities for the model is scaled according to Table 1.

	Scale factors	Values
Length	$\alpha = \frac{L_F}{L_M}$	100
Acceleration	$\frac{F}{M}$	1
Velocity	$V_M = \frac{V_F}{\sqrt{\alpha}}$	10
Time	$T_M \frac{T_F}{\sqrt{\alpha}}$	10
Force	$F_M = \frac{1}{\alpha^3}\frac{\rho_m}{\rho_f}F_F$	$\frac{1}{1025000}F_F$
Mass	$M_M \frac{1}{\alpha^3}\frac{\rho_m}{\rho_f}M_F$	$\frac{1}{1025000}M_F$

Table 1: Scaling factors. α is the scaling factor, ρ_m and ρ_f is the water density for the model and the full size structure. F is denoted for the full size, while M is model scale.

Chapter 3

3 Description of the Floating Substation

The Floating Substation's size and mass characteristics are described in this chapter. Sevan SSP has provided the data and information. The design of the floating unit is shown in Figure 4 and has the "typical" Sevan design, where the floater is circular with a constant diameter, except for the bottom part which has a larger diameter. There is however some differences from the typical design they deliver on their structures. This floater have smaller dimensions and a much lower freeboard.

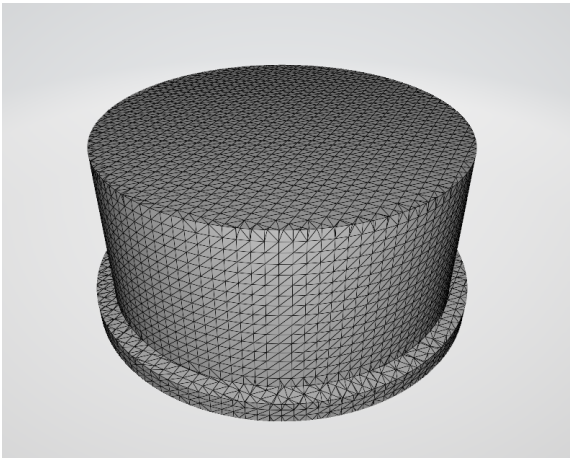

Figure 4: Picture of FEM model provided by Sevan SSP

3.1 Overview

During operation, the freeboard is set to be 11 meters, with a 14 meter draught. For an exposed location, where this unit will be located, it is therefore reasonable to assume that wave topping will occur. This was tested through a model scale where the dimensions are given below.

3.2 Dimensions and Mass Characteristics

The dimensions and intertia properties for the substation are provided by Sevan SSP 21^{th} of September 2022. Adjustments after this date is not included in this thesis. R_b is the radius of the "bilge keel" on the bottom of the construction, while H_b is the height of this "keel". R_w is the radius of the structure above the "keel", while H_w is the height of the unit from the top of the "keel" to the top of the structure.

	Value	Unit
R_b	27.5	[m]
H_b	2	[m]
R_w	25	[m]
H_w	23	[m]

Table 2: Dimensions full scale

	Value	Unit
R_b	0.275	[m]
H_b	0.02	[m]
R_w	0.25	[m]
H_w	0.23	[m]

Table 3: Dimensions model scale

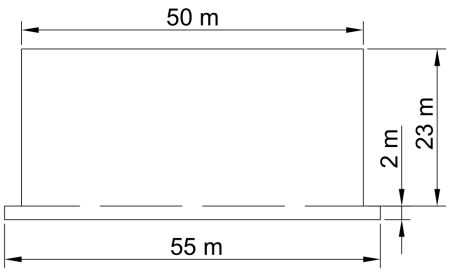

(a) Full scale model seen from the side

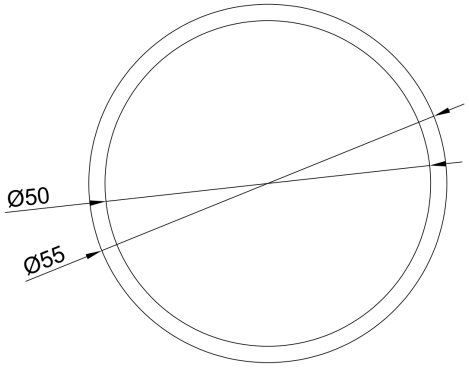

(b) Top view of full scale model

Figure 5: (a) displays the dimensions of the full scale model. (b) Shows how the unit looks like from the top.

	Value	Unit
M	30750000	[kg]
VCG	9.74	[m]
GM	5	[m]
R_{44}	14.43	[m]
R_{55}	14.43	[m]
R_{66}	17.68	[m]
I_{44}	6406250000	[kg m^2]
I_{55}	6406250000	[kg m^2]
I_{66}	9609375000	[kg m^2]

Table 4: Inertia properties full scale

	Value	Unit
M	30	[kg]
VCG	0.097	[m]
GM	0.05	[m]
R_{44}	0.144	[m]
R_{55}	0.144	[m]
R_{66}	0.177	[m]
I_{44}	0.657	[kg m^2]
I_{55}	0.657	[kg m^2]
I_{66}	0.985	[kg m^2]

Table 5: Inertia properties model scale

The moment of inertia is found using Equation 28. Where M is the mass, while Rij is the radii of gyration. Which is dependent on the geometry of the model.

$$I_{jj} = MR_{ij}^2 \tag{28}$$

Chapter 4

4 WAMIT

WAMIT version 7.4 is a linear potential flow solver which is developed for linear analysis for floating and submerged structures. The program will be used to evaluate the motions of the substation and thereafter the results will be compared with the experimental results.

4.1 Overview

WAMIT is a panel code program which solves the radiation and diffraction problem. The added mass and the damping is obtained from the radiation problem while excitation force comes from the diffraction problem. To obtain the rigid body motions, the combination of radiation and diffraction are combined, to present the RAOs.

The program consists of two sub-programs named POTEN and FORCE. Where POTEN solves for radiation and diffraction velocity potentials for the specified modes, frequencies and wave headings. FORCE computes the hydrodynamic coefficients, motions and first- and second-order forces. [5] WAMIT uses multiple input files, where the parameters in the files are changed according to the different aspects being analysed.

The main files used in WAMIT is the .gdf file, which contains information regarding number of symmetry planes and the mesh on the structure. The .frc file holds information abput the hydrodynamic parameters, and their options. The .pot file determines the environmental parameters. The fourth file is a .cfd file and provides parameters together with options for the analyses. The last file is the fnames.wam which specifies the mentioned files.

4.2 Inputs

One input that is assessed, in order to get the correct response in surge, heave and pitch, is the mass matrix. In WAMIT, the values from Table 5 are used. As the body is symmetric, the matrix becomes as shown in Equation 29. This means that I_{46}=I_{64}=0.

$$\mathbf{M} = \begin{bmatrix} M & 0 & 0 & 0 & Mz_g & 0 \\ 0 & M & 0 & -Mz_g & 0 & 0 \\ 0 & 0 & M & 0 & 0 & 0 \\ 0 & -Mz_g & 0 & I_{44} & 0 & 0 \\ Mz_g & 0 & 0 & 0 & I_{55} & 0 \\ 0 & 0 & 0 & 0 & 0 & I_{66} \end{bmatrix} \tag{29}$$

The restoring matrix is not provided, as WAMIT calculates it from the geometry of the model. However, the input from the external stiffness matrix due to horizontal mooring lines must be given manually. The matrix becomes as in Equation 30. The values of the horizontal stiffness are given in section experimentsss - må endres

$$\mathbf{C^E} = \begin{bmatrix} c_{11} & 0 & 0 & 0 & c_{15} & 0 \\ 0 & 0 & 0 & 0 & 0 & 0 \\ 0 & 0 & 0 & 0 & 0 & 0 \\ 0 & 0 & 0 & 0 & 0 & 0 \\ c_{51} & 0 & 0 & 0 & c_{55} & 0 \\ 0 & 0 & 0 & 0 & 0 & 0 \end{bmatrix} \tag{30}$$

4.3 Mesh sensitivity study

In order to find the optimal number elements for the analyses in WAMIT, a mesh sensitivity study has been performed. The geometry data file, *.gdf*, were generated using a Python script, dividing the structure into several panels. Where the number of panels can be adjusted by changing number of azimuthal, radial and vertical sections. The number of panels are the results of the following sectioning of the vertical and horizontal division.

678 panels	6, 2, 2, 6
1440 panels	10, 5, 5, 10
2640 panels	15, 10, 10, 20
3552 panels	20, 12, 12, 30

Table 6: Sectioning of panels

The structure is symmetric about the x and y axis and this helps in regards of computational time, as only a quarter of the model was modeled. Whereas the number of panels described is the total number of panels for the whole body. It is important to note that only the submerged part of the body is meshed. This can be seen from the figures below, where the model have a draught of 0.14 meters.

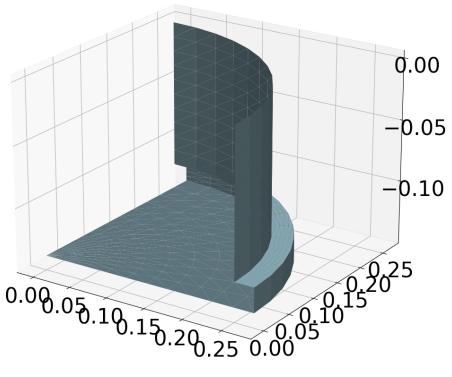

(a) Submerged mesh of one model

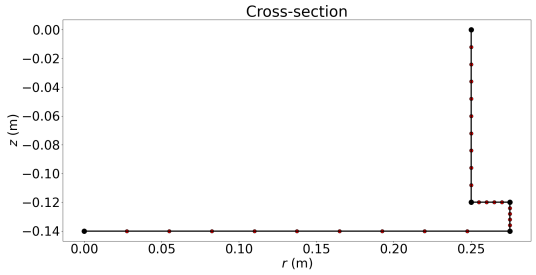

(b) Cross section of model

Figure 6: (a) displays the submerged mesh and has a total of 1440 elements, and is created by the use of a Python code. (b) displays the cross section of the model in regards of sectioning on the model.

For the following figures, only the differences as a results of the different panels numbers between the models will be discussed. The shape of the graphs, and the reasoning for this will be discussed later. The analyses have been performed without the external stiffness from the moorings, in finite water.

The added mass and damping in heave is shown below in Figure 7. There are some differences in added mass between the different number of panels, especially for the models with coarser mesh. Compared to the model with 3552 panels. For some reason the model with 2640 panels greatly deviates from the other models. It was not possible to find any irregularities in the execution of the analysis which could account for this. For damping in heave there is negligible differences between the different models with 678, 1440 and 3552 panels. While the model with 2640 panels are a bit offset for the kD number between 3.8 and 1.2

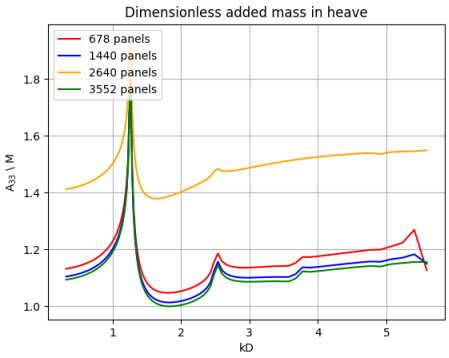

(a) Mesh sensitivity study of added mass in heave.

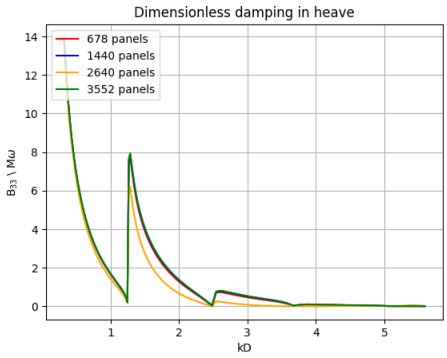

(b) Mesh sensitivity study of damping in heave.

Figure 7: (a) displays the mesh sensitivity study of added mass in heave. (b) displays the mesh sensitivity study of damping in heave.

In Figure 8 there are some deviations for the model with 2640 panels for the added mass in surge, while the other models are on top of each other. For damping the situation are identical with a slight offset of the model with 2640 panels compared to the others. In pitch there is a large offset for the model with 2640 panels both in added mass and damping, while the three other models are relatively similar. Where the differences between 1440 panels and 3552 panels are small.

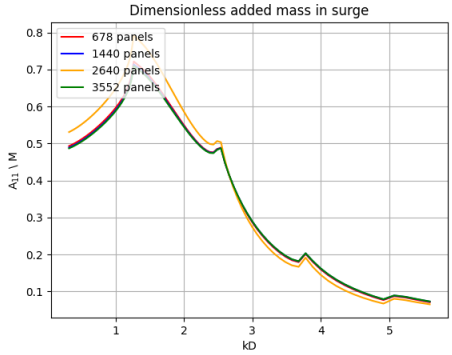

(a) Mesh sensitivity study of added mass in surge.

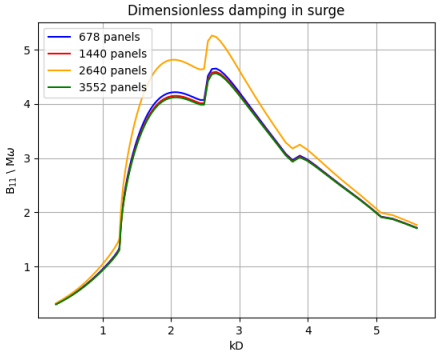

(b) Mesh sensitivity study of damping in surge.

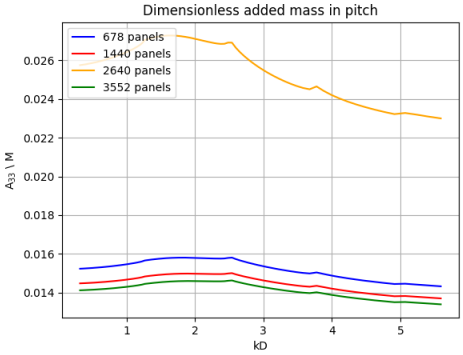

(c) Mesh sensitivity study of added mass in pitch.

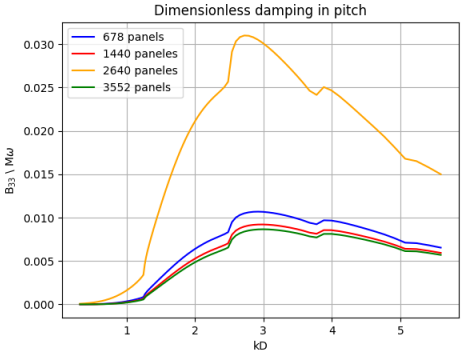

(d) Mesh sensitivity study of damping in pitch.

Figure 8: (a) displays the mesh sensitivity study of added mass in surge. (b) displays the mesh sensitivity study of damping in surge.(c) displays the mesh sensitivity study of added mass in pitch. (d) displays the mesh sensitivity study of damping in pitch.

In surge there is a peak at kD around 1, depending on the number of panels on the model. Where the model with 2640 panels have a higher peak at a slightly lower kD value. While the three other models are almost identical. In pitch the same results can be seen regarding the peak and the kD value, whereas there are some differences between the models and their response in pitch. Where the model with 3552 panels have the lowest response. The heave motion are almost identical between the models, except for the model with 2640 panels, where local peak is set at a slightly lower kD, whereas the global peak is much higher.

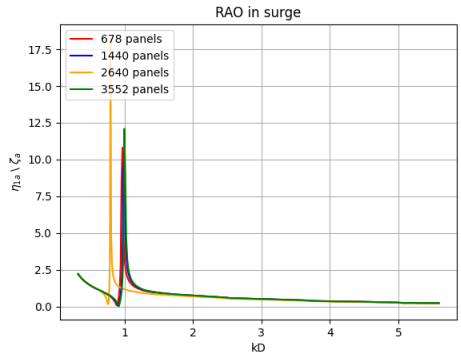

(a) Mesh sensitivity study of surge RAO.

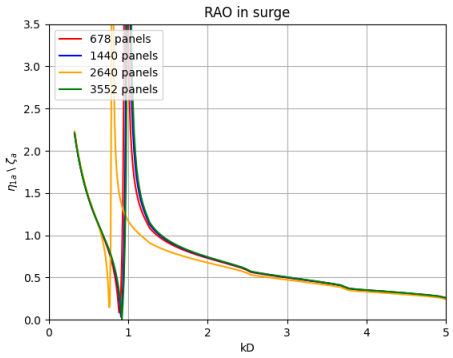

(b) Zoom-in of surge RAO

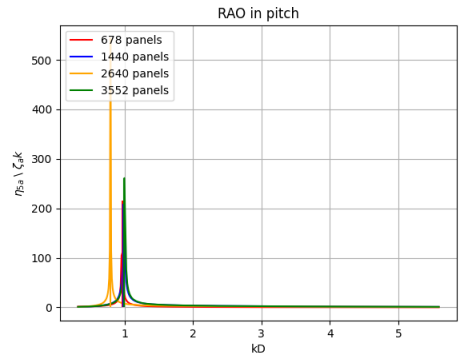

(c) Mesh sensitivity study of pitch RAO.

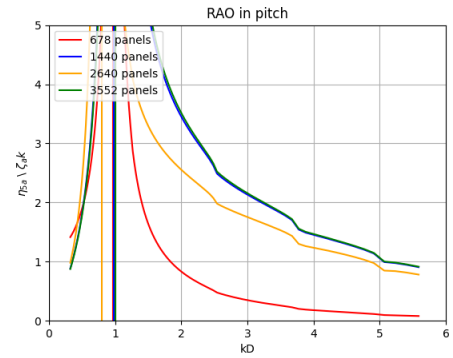

(d) Zoom-in of pitch RAO

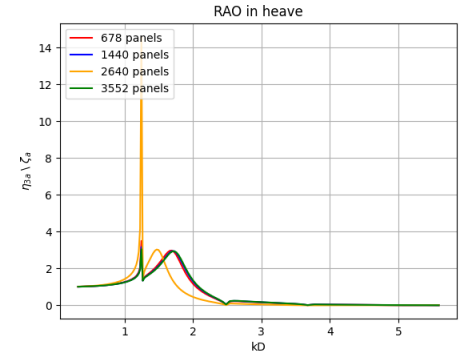

(e) Mesh sensitivity study of heave RAO.

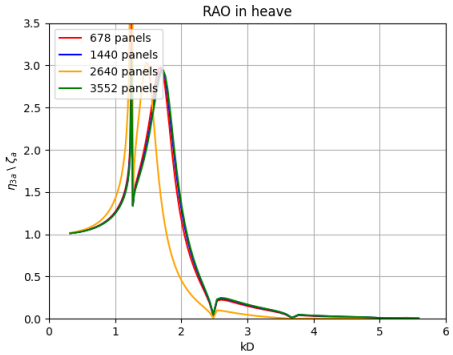

(f) Zoom-in of heave RAO

Figure 9: (a) displays the surge RAO. (b) displays the zoom-in of the surge RAO.(c) displays the pitch RAO. (d) displays the zoom-in of the pitch RAO.(e) displays the heave RAO. (f) displays the zoom-in of the heave RAO.

The results have in common that they indicate that the models with 1440 and 3552 panels provides similar results, and there is minimal difference between the two models. In regards of computational time, the model with 3552 panels uses significantly longer time to finish the analyses than the model with 1440 panels. The conclusion is therefore to use the model with 1440 panels for further studies.

4.4 Analyses

Multiple aspects will be investigated using different models with different settings in WAMIT. There will be provided a short description of the different analyses below. The model study examines the impact of a larger keel. While the draught study investigates how different drafts and inertia properties affects the motions in surge, heave, roll and pitch. The pre-tension study provides insight in how the mooring affects the motion of the model. The same aspects will be used in the experimental model tests in Lilletanken, in an attempt to replicate the results from WAMIT.

4.4.1 Model study

In order to evaluate how the bilge keel affects the response, two different models of the keel will therefore be compared.

- **Model with regular bilge keel**: The lab model with a keel radius of 0.3 meters.
- **Model with larger bilge keel**: The lab model with a keel radius of 0.275 meters.

4.4.2 Draught study

The draft was decreased, with following changes in the mass, vertical center of gravity and radii of gyration to account for the change in displaced volume.

- **Draught = 0.14 m**: Original draught.
- **Draught = 0.17 m**: Increase of draught to 0.17 m.

4.4.3 Pre-tension of springs study

The model was evaluated with two different values of pre-tension for the springs at the original draft.

- **Pre-tension = 4 N**: Original pre-tension in moorings.
- **Pre-tension = 7 N**: Increase pre-tension in mooring by 75%.

4.4.4 Rundown of Configurations

In total there will be performed six configurations, which will be referred to as:

1. **Configuration 1**: 4 N pre-tension on mooring with a keel radius of 0.3 meters and a draught of 0.14 meter.
2. **Configuration 2**: 4 N pre-tension on mooring with a keel radius of 0.275 meters and a draught of 0.14 meter.
3. **Configuration 3**: 4 N pre-tension on mooring with a keel radius of 0.3 meters and a draught of 0.17 meter.
4. **Configuration 4**: 4 N pre-tension on mooring with a keel radius of 0.275 meters and a draught of 0.17 meter.
5. **Configuration 5**: 7 N pre-tension on mooring with a keel radius of 0.3 meters and a draught of 0.14 meter.
6. **Configuration 6**: 7 N pre-tension on mooring with a keel radius of 0.275 meters and a draught of 0.14 meter.

4.4.5 Experimental reproductions

Experimental tests will be performed in an attempt to replicate the results from WAMIT. A numerical model will be made equivalent to the experimental model, corresponding to the different models. The analyses have been performed with a channel width equivalent to Lilletanken at 2.5 meters, with a water depth h= 0.7 m. For the performed tests, the water depth changes from infinite water depth to finite water depth at 0.947 seconds. This equals to a kD value slightly higher than 2.

Chapter 5

5 Experimental set-up

The experiments was performed in Lilletanken at NTNU. The tank is 25 meters long, 2.5 meters wide with a maximum depth of 1 meter. Due to limitations of the wave maker, the water depth was set at 0.7 meter for the experiments. As there is fresh water in the water tank, the density is assumed to be 1000 kg/m^3

The experimental setup in the tank consisted of:

- Two wave-probes located 4 meters from the wave-maker.
- Two wave-probes located 8 meters from the wave-maker.
- Two wave-probes located 15.275 meters from the wave-maker.
- Model is located at pit centre, 15.275 from the wave maker.
- Four wave probes located at 0°, 90°, 180°, 270° on the model to measure the wave topping.
- Four mooring lines are attached to the model at a 45°interval, 0.19 m above the bottom of the structure
- A perforated parabolic beach installed at the end of the tank, to reduce wave reflection.

The wavetank setup can be seen in Figure 10.

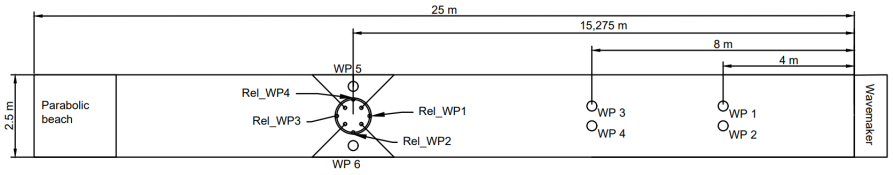

Figure 10: Experimental test set up in Lilletanken.

The reason for using two wave probes located at 4 meter, 8 meter and 15.275 meters is to increase the accuracy of the results for the waves.

For measuring of motions six degrees of freedom on the model, Oqus was used. The program uses optical tracking, which provides provides position and motion of moving objects at high accuracy. This is achieved by using cameras and reflective markers [13]. In addition there was mounted 3 accelerometers on the model, in case Oqus failed. They are mounted at 0°, 90° and in the center of the model. The forces on the mooring lines will also be measured, by the use of force rings.

In Figure 11a one can see screws at the green bilge keel, at the same placement where the relative wave measure touches the keel. This makes it possible to adjust the diameter of the keel. The four grey bulbs are used by the Oqus system to track the motions of the structure. As the measure points has to be located with some distance between each others, this lead to the use of the "triangular" arm. At Figure 11d the adjustable lot is located at a different placement, due to slight changes in the gravity of center when lot was added to the model at larger draughts.

(a) Picture of configuration 1 before it is put into the tank.

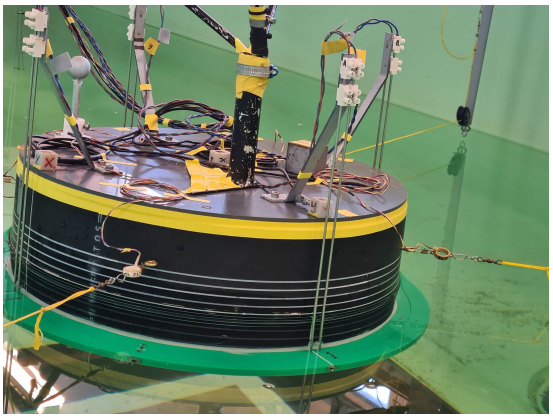

(b) Configuration 1 in the tank, with a draught of 0.14 meter.

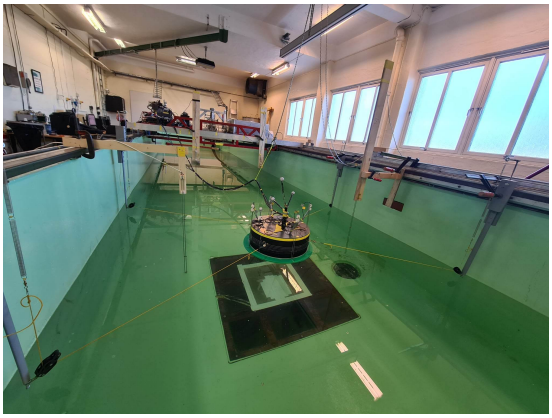

(c) Overview of configuration 1 moored in the tank.

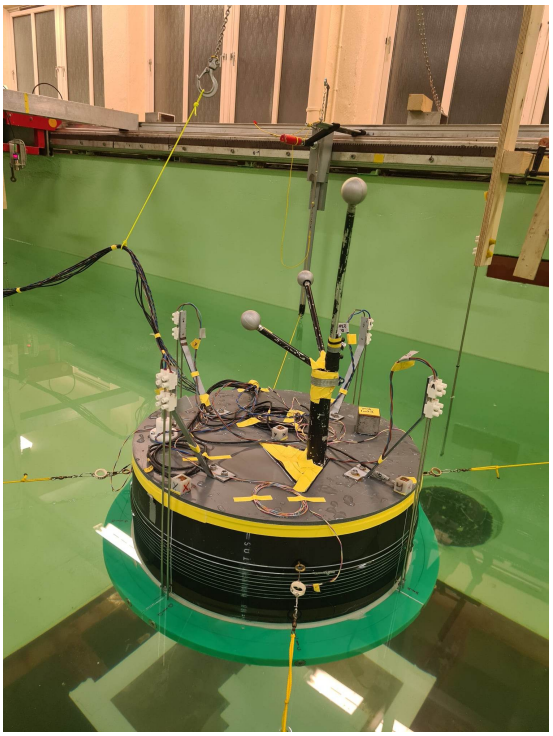

(d) Configuration 5 in the tank, with a draught of 0.17 meter.

Figure 11: Pictures of experimental models providing a better overview of the model and the experimental setup the wave tank.

5.1 Mooring

Using information provided by Sevan for the full size model, the pre-tension for the model is calculated to be around 4 N/m, and it was therefore assumed that springs with a stiffness of 10 N/m would be sufficient. However this proved to be wrong due to the elongation of the springs. Instead springs with a stiffness of 50 N/m were mounted in series, equaling to 25 N/m. The moorings were attached to the model 0.05 meter above the waterline at 0.14 meter draft.

Figure 12: Close up of the connection between the springs. Two 50 N/m springs in series creating a 25 N/m spring.

The mooring lines adds some additional restoring to the model, and the values of those equations are given by the equations below. Where k_x and k_y is the components of the spring, in x- and y-direction. D_w is the diameter of the structure, and a is the distance between the vertical point of gravity and mooring lines.

$$C_{11} = 4k_x \tag{31}$$

$$C_{55} = F_{pre}D_w \tag{32}$$

$$C_{15} = C_{51} = 2k_x a \tag{33}$$

The values from the equations above is used in Equation 30 to account for the external stiffness from the mooring lines in numerical analyses.

5.2 Tests

5.2.1 Regular wave tests

Six different wave steepness were chosen for the regular wave tests, and those were: $\epsilon = 1/40$, $\epsilon = 1/35$, $\epsilon = 1/30$, $\epsilon = 1/25$, $\epsilon = 1/20$ and $\epsilon = 1/100$. Minimum period was set at 0.6 seconds, while the maximum period was set at 2 seconds. At three given wave periods, the corresponding wavelength λ and wave height H can bee seen in Table 7. Where the table shows the smallest and largest wave, as well as the period where the water depth becomes finite.

		ϵ=1/20	ϵ=1/25	ϵ=1/30	ϵ=1/35	ϵ=1/40	ϵ=1/100
kD	λ [m]	ζ [m]	ζ [m]	ζ [m]	ζ [m]	ζ [m]	ζ [m]
5.5895	0.562	0.014	0.011	0.009	0.008	0.007	0.003
2.1095	1.489	0.037	0.03	0.025	0.021	0.019	0.007
0.503	6.246	0.156	0.125	0.104	0.089	0.078	0.031

Table 7: Regular waves presented

5.3 Error sources

Lab experiments are proned to both bias and precision errors which pollutes the results. Typical bias errors and their possible effects on the results will be discussed.

5.3.1 Bias errors

Typical bias errors are the result of simplifying the model, and those errors are known from the start of the experiment. A list of possible bias errors where known in advance, and those will be further on elaborated on.

Incident waves

The waves for the experiments were created using a Matlab code. In order to ensure that the waves from the wave-flap were in line with the theoretical waves, the results were compared. Where the measured wave height are the average of the values measured from WP5 and WP6. These wave-probes are located at the same distance from the wave-flap as the model during the experiments, not accounting for surge in the model. The measured wave heights corresponds nicely to the theoretical. However the incident waves are a bit over predicted at ϵ=1/100 from kD values from 2 til 0. This does not occur for the wave steepness-es between 1/40 to 1/20. Which might indicate that the wave maker were not properly calibrated at for the 1/100 steepness. As the same results can be seen from the measurements from WP3 and WP4 at ϵ= 1/100. This can be seen in Figure 32 in the Appendix.

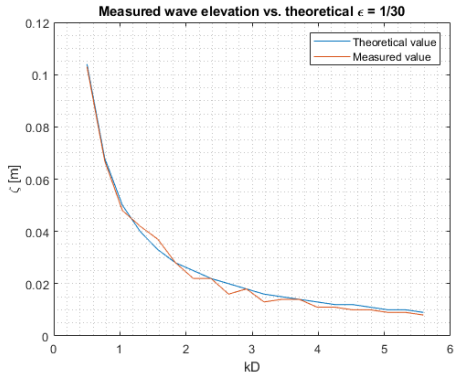

(a) Theoretical waves compared to measured waves at $\epsilon = 1/30$

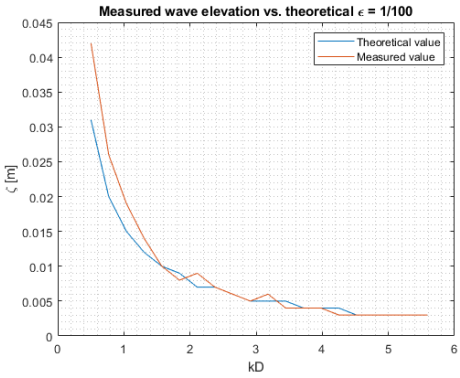

(b) Theoretical waves compared to measured waves at $\epsilon = 1/100$

Uncertainties in wave probes and wave maker

The wave probes measure wave height from the rise and fall of water level using the conductivity of water. With the conductivity being influenced by both changes in temperature and pollution of the water, especially oil spills, there can be errors in the measurements. However, such errors did not occur during the experiments as the water temperature did not fluctuate too much. It is documented that even a small change in temperature has the ability to affect both the density and viscosity of the water. From a table in [4], the uncertainty of density in fresh water is calculated to be $\pm 2.8 \cdot 10^{-8}$ [m^2/s] while the uncertainty in viscosity is calculated to be ± 0.18 [kg/m^3]. This provides us with possible deviations of 2.8 % for ν and 0.018% for ρ per degree change in water temperature. Since there were no noticeable temperature changes during the experiments, it is unlikely that this was the reason for the measurements at $\epsilon = 1/100$ being off. Nevertheless, the wave probes were calibrated before each run to account for any minimal changes in temperature.

The wave-flap used in the towing tank is of the piston type. It consists of four cylinders that pushed the plate, however only three of them were working during the experiments. This is suspected to potentially result in a slightly askew piston motion, which might induce some tank wall resonances. As it was observed at

With the kind of wave-flap used, there is leakage into the space behind the piston. Which might decrease the water level in the tank if the pumps installed were not working properly. The operation system to the pumps were affected by the explosions due to building processes outside of the building. This had the potential to influence the water level if the hiccup in the system were not observed right away.

Tank leakage

The tank slightly leaks, in addition to the leakage behind the wave-flap. As the water level in the tank were not the same in the evening, as it was in the morning the same day. The water depth varied with 0.01 meter during a 24 hour time span. The difference for the produced wave heights proved to be insignificant.

Tank wall effects

Performing experiments in a narrow tank will result in wall reflections from both the sides and the tank wall ends. This was accounted for through a long pause between each set of waves. In post processing this was also accounted for by using a steady state time window period before the reflected waves reached the model. While the reflections from the side walls were not possible to account for.

Deviations in the model

The model was constructed from parameters provided by Sevan. Both the vertical center of gravity(vcg)and radii of gyration ended up on deviating on the scaled model compared to the provided parameters. The model ended up on being 0.72 kg lighter than estimated at 0.14 meter draft. While the vcg ended up on being 0.013 meter higher than anticipated. These changes are important regarding the motions of the structure, especially for the numeric simulations. There are some inaccuracies on the model, in regards of the circularity for the construction as the black part of it was cut out from a pipe.

There are also an error source due to the instrumentation cables hanging from the model. The cable bundle might have affected the results, due to the tension from the line and the angel it is hanging from, seen in Figure 14. Where this especially might have affected the rigid body motions in yaw and roll, and partially in pitch.

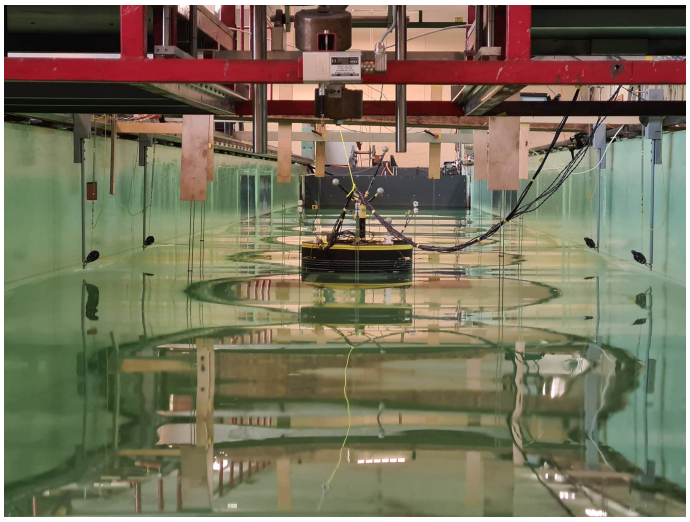

Figure 14: Picture from behind showing the bundle attached to the model. The bundle can also be seen in the prevous pictures.

Mooring lines

The mooring was attached to the model at 45° intervals, and springs were used to get the desired pre-tension. When the manual adjusting of the mooring lines took place, it was important to keep the position of the model in mind in order for it to

stay in the wanted position. The attempt to obtain an equal pre-tension in the lines proved difficult, and the deviation between the spring with the lowest and highest tension were at the most 0.4 N. During the experiment it was observed that the mooring lines were not stiff enough for the model at 0.17 meter draught as slack occurred at the springs for the most severe wave periods and sea states.

5.4 Post-processing

The post-processing of the data from the experiment have been quite time consuming, and a lot of time have been spent in order to acquire the desired results.

The regular wave tests were performed by repeating each wave period 60 times, with five minutes breaks in between for the given periods and wave steepnesses. The response for each wave period was extracted from the time series in the wave probes. In order order to retrieve the data corresponding to the correct wave period period, the trigger signal from the wave-flap was used. The retrieved data was then filtered through a band-pass filter, removing noise and higher order methods by implementing cut-off periods. After the data had been filtered, a steady state window for each were then chosen. Which from the use of the trigger signal was calculated to use data from the period between number 25 and 45. In Figure 15 one can observe two red vertical lines with a blue dot on the x axis, indicating start and stop of the wave-flap. Whereas the the red dot on the line marks when the data collection start and end. During those periods, including ramp up and down, the steady state is collected.

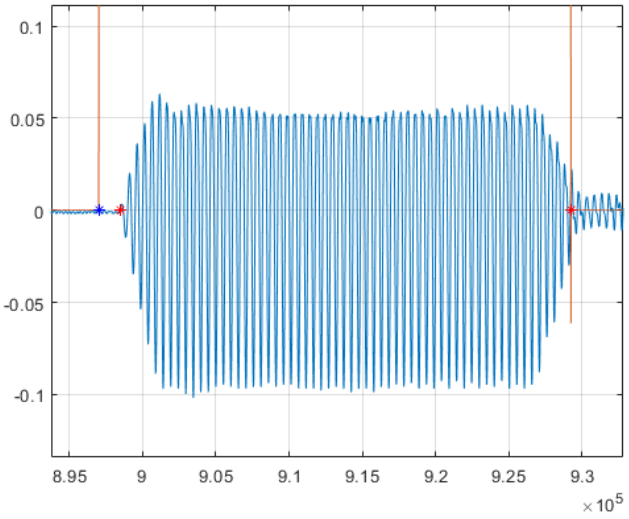

Figure 15: Filtered data for wave probe 5 in the wavetank, collecting regular wave data from regular waves

From the steady state window, the mean wave heights are found by measuring the peaks. The mean wave height was used to calculate the response amplitude operators. Where the values/response captured by the Oqus system are divided by the mean wave height.

Chapter 6

6 Parameter study

In this section the results from the draught, bilge keel and pre-tension analyses are presented. The effect of the draught on the body motions were conducted in order to increase the understanding of motions for the structure, as well as examining how the keel radius plays affects the motions combined with changes in the pre-tension of the mooring. For the changes of draughts, the vertical center of gravity and other affected variables was changed. The analyses were run for finite water.

6.1 Bilge keel, draught and pre-tension study

From the figures it is observable that the bilge keel affects the rigid body motions. The natural period in surge, heave and pitch increases with a larger keel, as a result of the additional added mass effect. Which is the reason why Config 1 has resonance at a lower kD value than Config 2 in surge and pitch. In surge and pitch the natural period occurs at a kD value at around 0.8. While in heave it is 1.3 for Config 1. For Config 2 resonance in surge and pitch occurs at kD equal to 1.1, and heave equal to 1.3. With surge and pitch resonance occurring at the same period, it is a indication that there is a probability of encountering Mathieu instability. With increased keel radius, the viscous flow separation will increase around the keel. This will cause significant damping effects on the model, which is not captured by WAMIT. Especially heave and pitch will be affected by this, and it is expected that the experimental results will differ from the numerical results.

The same observations seen in Config 1 and 2 can be seen for Config 3 and 4 in the draught study. Where Config 3 which has the largest keel have a higher natural period, compared to Config 4. Which indicates that the larger keel makes the model more mass dominated. At a deeper draught, the RAOs are not significantly different from Config 1 and 2. The minimal change in the vertical center of gravity or the values of I_{44}, I_{55} and I_{66} may account for this. Nonetheless the resonance period did shift to left, as expected.

In the pre-tension study, the results are not to different from the model study. Indicating that the effects of the higher pre-tension are not captured in the response amplitude operators from the analyses.

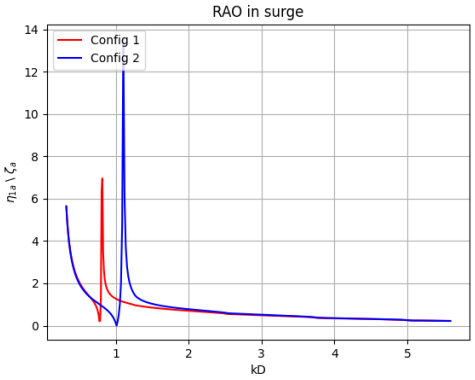

(a) RAO in surge for configuration 1 and 2. Larger keel radius gives a higher resonance period.

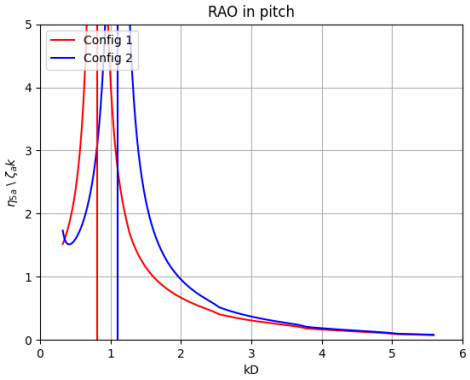

(b) RAO in pitch for configuration 1 and 2. Larger keel radius shifts the resonance period to the left.

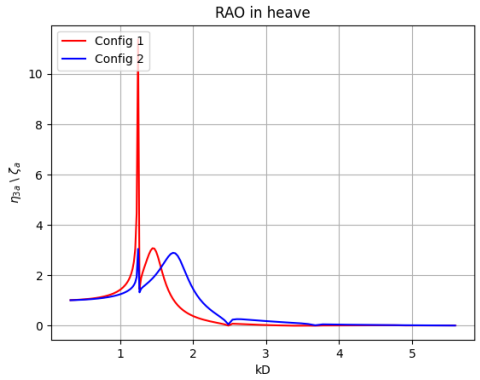

(c) RAO in heave for configuration 1 and 2. No difference in resonance period.

Figure 16: RAOs for configuration 1 and 2.

Draught study

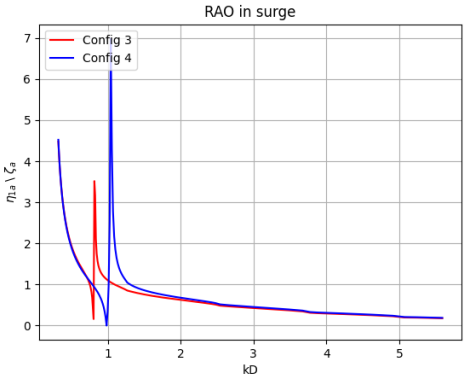

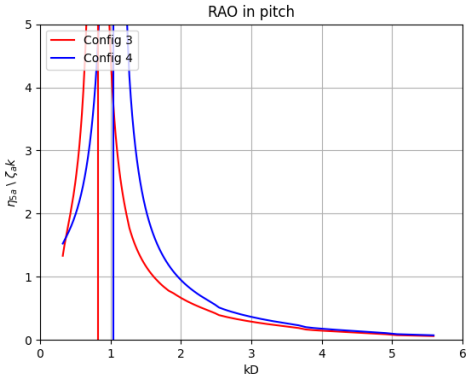

(a) RAO in surge for configuration 3 and 4. Minimal shift to the left in resonance periods compared to configuration 1 and 2.

(b) RAO in pitch for configuration 3 and 4. Minimal shift to the left in resonance periods compared to configuration 1 and 2.

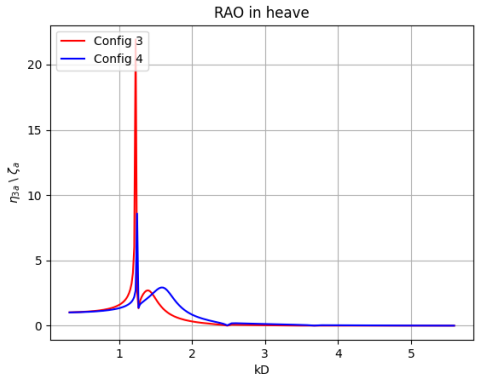

(c) RAO in heave for configuration 3 and 4. No difference compared to configuration 1 and 2.

Figure 17: RAOs for configuration 3 and 4.

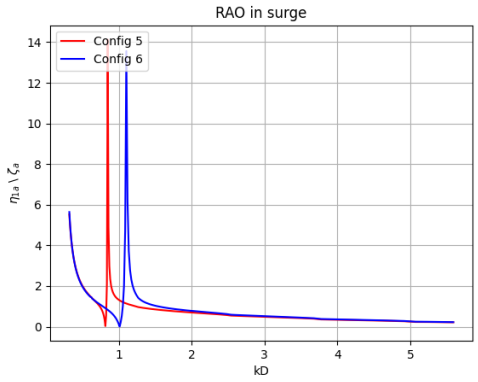

(a) RAO in surge for configuration 5 and 6. No observed difference compared to configuration 1 and 2.

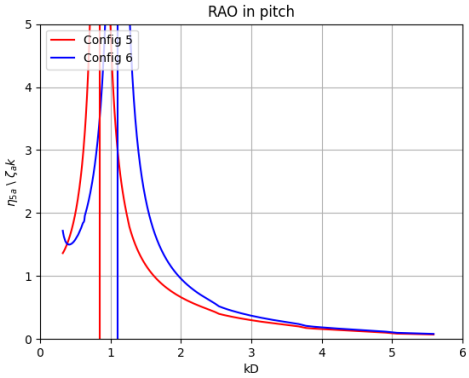

(b) RAO in pitch for configuration 5 and 6. Looks identical to configuration 1 and 2.

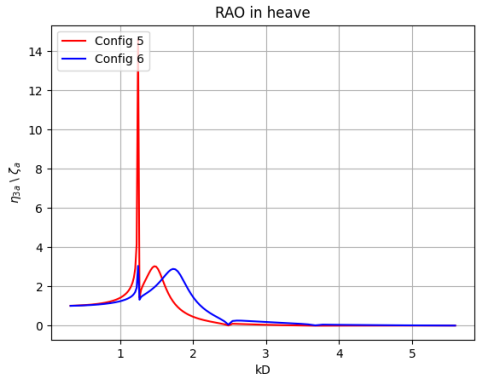

(c) RAO in heave for configuration 5 and 6. Similar to configuration 1 and 2.

Figure 18: RAOs for configuration 5 and 6.

6.2 Added mass and damping coefficients

For the six configurations, the added mass and damping coefficients in surge, heave and pitch are presented. Config 2 and Config 6 have almost virtually the same results, for all the variables of the added mass coefficients. However this is not the case for the dimensionless damping. There was spent a great amount of time control checking for errors, as the results seemed unusual. Unfortunately no errors were found.

The added mass and damping coefficients differs for the different configurations. In surge the added mass increases more for the configurations with a large keel at longer wave periods, compared to the models with smaller keel. They all have a peak at a kD period at 1.4. The dimensionless damping at this period is low.

In heave the added mass is larger for the configurations with a larger keel, due to the geometry. The added mass coefficient have a slight decline as the wave periods

increases until the resonance frequency is met, where it spikes. Whereas the damping at the added mass peak is low. However it does not account for viscous damping. Configuration 5 and 6 differs from the others as they do not have any resonance frequencies for damping in heave. It is likely this is due to the mooring stiffness.

The added mass in pitch stays approximately constant, and is not affected by the wave period. For a larger keel, the added mass are higher than for the models with smaller keel. The damping in pitch is especially of interest in regards of Config 5 and 6, as those differs from the other configurations by having an almost horizontal line. This indicates that the damping will be the same, regardless of the period when viscous damping is not accounted for. Again, a larger keel provides a higher damping coefficient. With a larger variation in the damping depending on the period.

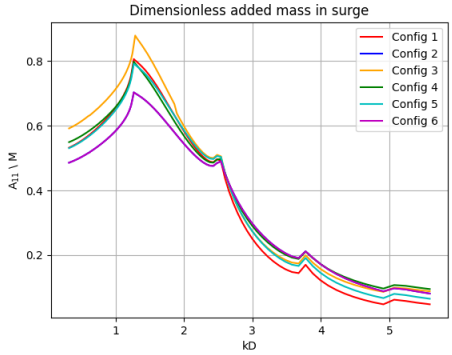

(a)

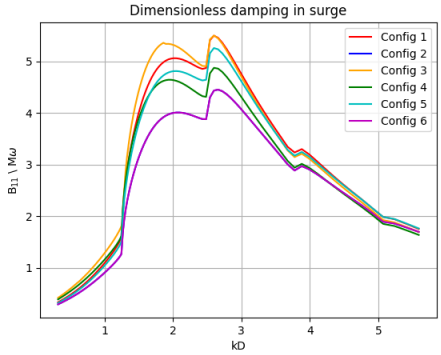

(b)

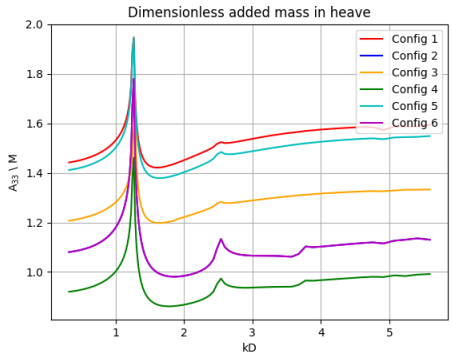

(c)

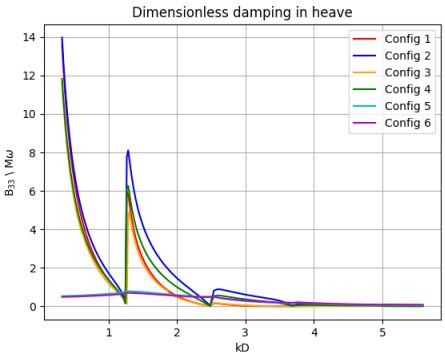

(d)

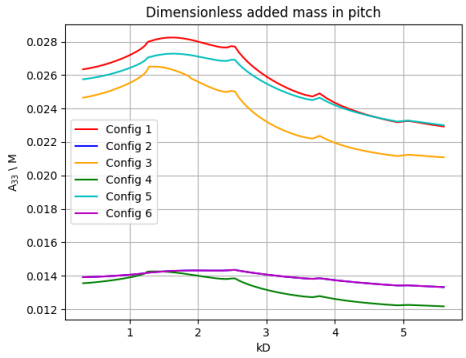

(e)

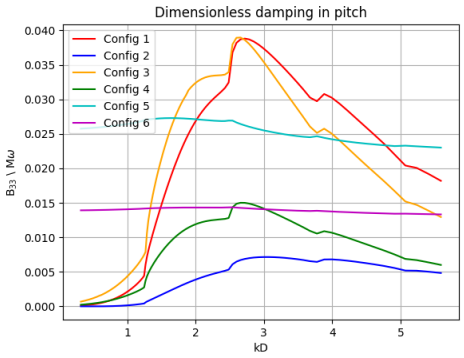

(f)

Figure 19: Added mass and damping coefficients in the parameter study for the different configurations.

6.3 I55 study

There have also been conducted a study to observe how changes in the I55 value affects the rigid body motions. I55 is the moment of inertia in pitch. The configurations with low I55 have a 20 % lower value than the experimental model, while the configurations with high I55 have a 20 % higher value. As expected will this effect the period at which the resonance occurs at. Where a higher moment of inertia leads to a higher resonance period, and vice versa in pitch. This also affects the resonance period in surge. However there are almost no difference in the heave motion with the change of the I55 value.

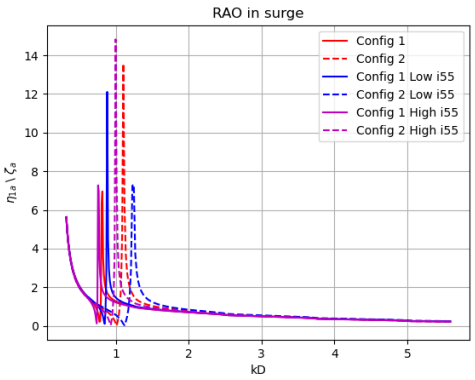

(a) Surge RAO

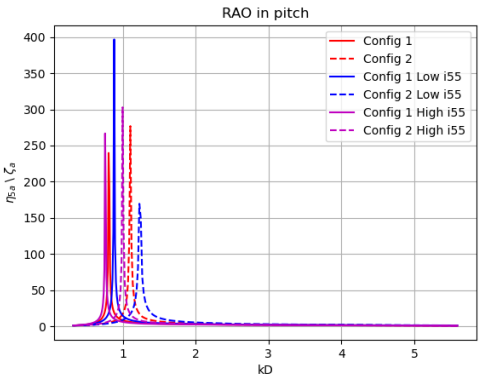

(b) Pitch RAO

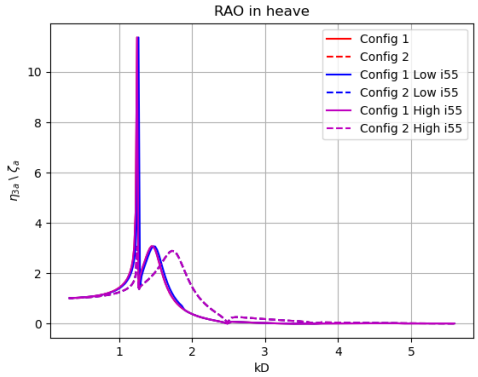

(c) Heave RAO

Figure 20: RAOs for the different I55 values in surge, heave and pitch. Increase in I55 shifts the resonance period to the left in surge and pitch, and vice versa. Resonance in heave is unaffected by the changes.

7 Results

Within this chapter, the results from the experiments are presented. The experimental results are presented in model scale, with a scaling factor $\alpha = 100$. Which easily transforms the the periods used in the experiments to full scale periods by the use of the relation $T_F = \sqrt{\alpha} \cdot T_M = 10 \cdot T_M$. Where the subscripts F and M denotes the full scale and mode scale.

7.1 Regular wave results

The RAOs from the experiments are plotted, together with a numerical analysis. As seen in the Figure 33, the differences between the numerical configurations are minimal, and therefore only one numerical condition will be used when plotting the different configurations at the same wave steepness. The results will be presented for the same configuration at the different wave steepnesses, and also for the different configurations at the same wave steepness on order to make it easier to compare how the different configurations responds in the different waves.

The values on the x - axis are the results of wavenumber multiplied with the diameter of the model. The values are hard to interpret in regards of correlating their number to a more useful value, such as seconds. In Table 8 it is therefore presented table where the kD values and their respective period in seconds are presented. Due to the nature of using wavenumber k, the measure points are not spread evenly. With them being closer at lower periods with increasing steps as the periods increase.

kD	t [s]
5	0.634
4.5	0.669
4	0.709
3.5	0.758
3	0.819
2.5	0.897
2	1.003
1.5	1.158
1	1.419
0.5	2.006

Table 8: kD values and corresponding periods in seconds

7.1.1 Configuration 1 and 2

The numerical analyses correlate with the experimental results in surge for both Configuration 1 and 2. It is interesting to observe how the experimental results at ϵ=1/100 follows the numerical results for both configurations, including the local peak at kD 1.4 for Config 2. Especially in surge. This suggest that the motions for this steepness exhibit a higher degree of linearity compared to the other wave

steepnesses. Which was partially expected at the given wavelengths. The local drop at kD period of 1 indicates that there might occur secondary forces for both configurations at this period. This effect is not as significant for the other wave steepnesses. In pitch, ϵ=1/100 follows the numerical results due to the higher extent of linearity. This result in what seems to be a higher convergence value, compared to the steeper waves. Which is likely caused by the reduced viscous damping at this steepness. In heave the results converges towards a value of 1 at lower kD periods. The results for ϵ=1/100 deviate a bit from the other experimental tests, especially for Config 2. Where it might be due to the cancellation of the Froude-Krylov force, combined with non linearities such as the viscous damping. At ϵ=1/100 there are tendencies that it will converge towards a response of 1.5.

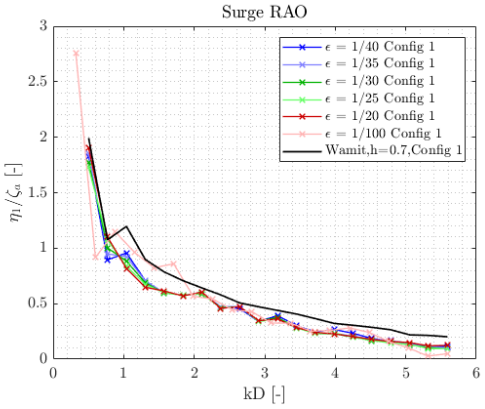

(a) Surge RAO Config 1

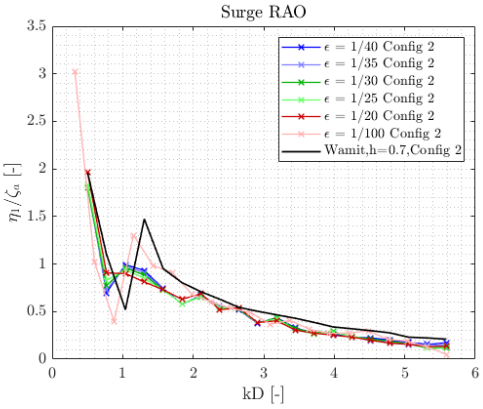

(b) Surge RAO Config 2

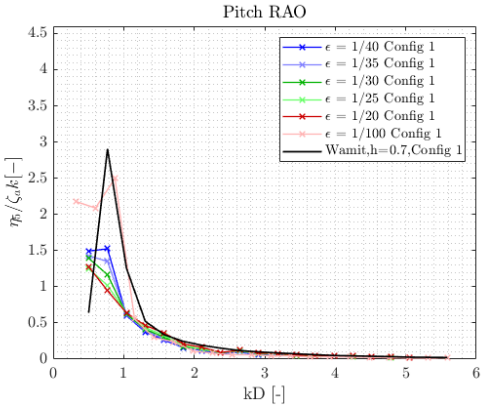

(c) Pitch RAO Config 1

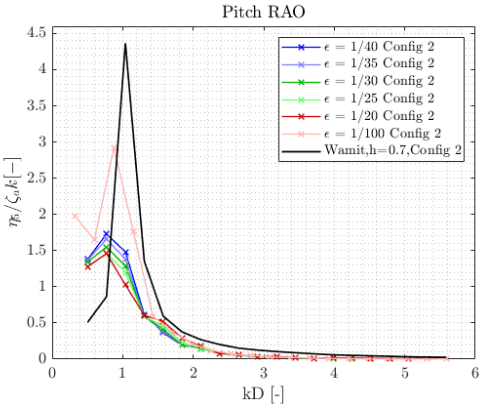

(d) Pitch RAO Config 2

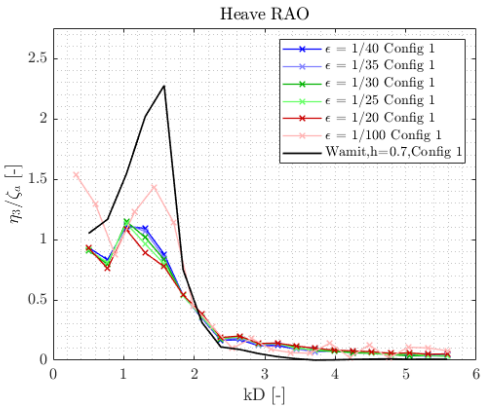

(e) Heave RAO Config 1

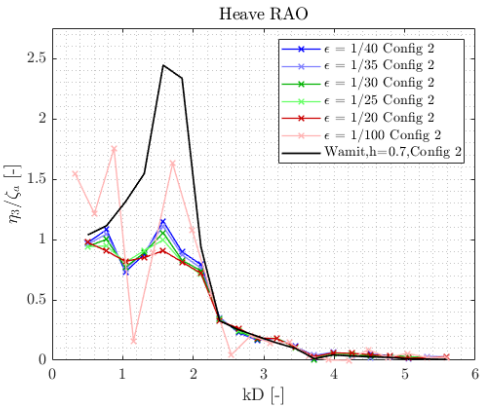

(f) Heave RAO Config 2

Figure 21: RAOs for configuration 1 and 2.

7.1.2 Configuration 3 and 4

For Configuration 3 and 4, the responses from the numerical analyses coincide with the experimental tests. With slightly lower responses in surge and pitch for Configuration 3 compared to Configuration 4. The spike in surge in the numerical analysis for configuration 4 is due to a convergence error. In pitch at ϵ=1/100 for configuration 4, the response at resonance period is caused by the linearity in the waves, reducing the viscous damping. In heave there is a convergence error for the numeric analysis, causing the flat top in configuration 3. Regarding heave, there is a greater response at the resonance period for configuration 3 compared to configuration 4. It appears that there are no resonance periods for wave steepnesses between 1/20 and 1/40 in configuration 4. For ϵ=1/100 the results deviate from the others. Indicating that some of the assumptions regarding Config 2 also applies for configuration 4.

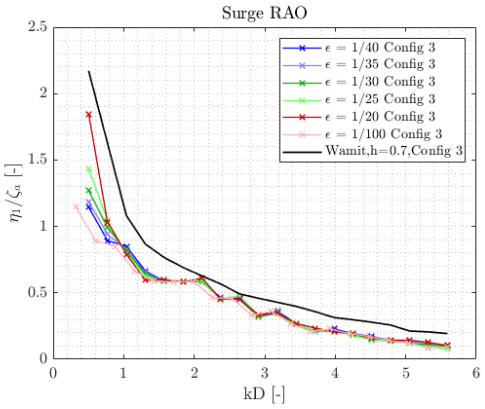

(a) Surge RAO Config 3

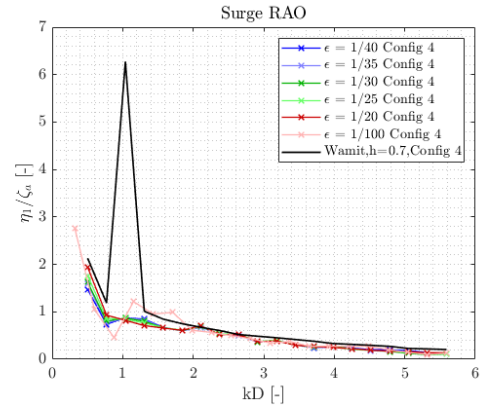

(b) Surge RAO Config 4

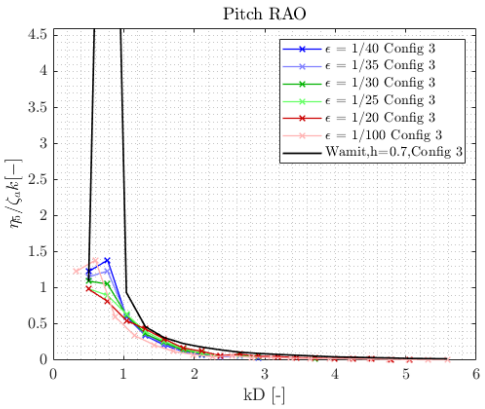

(c) Pitch RAO Config 3

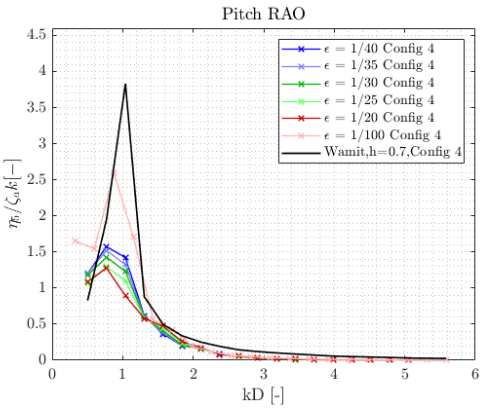

(d) Pitch RAO Config 4

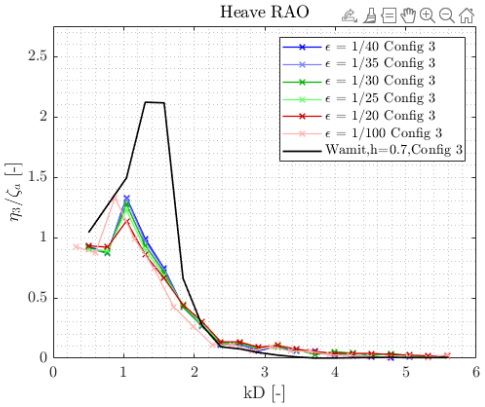

(e) Heave RAO Config 3

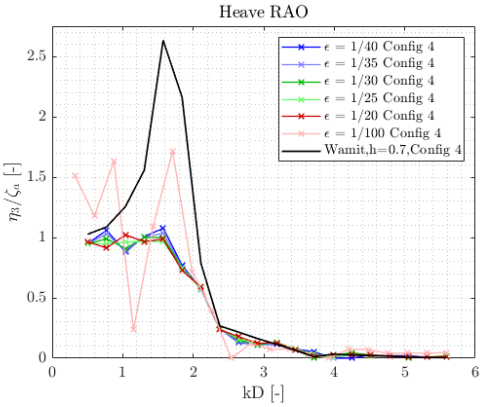

(f) Heave RAO Config 4

Figure 22: RAOs for configuration 3 and 4.

7.1.3 Configuration 5 and 6

There is a slight difference between Config 5 and 6 in surge. The numerical simulation of Config 6 have a local peak at kD equal to 1.4, which is not captured by the experimental results. In pitch the response at ϵ=1/100 coincide with the numerical results, which is not the case for the other steepnesses. This is likely due to a combination of the wavelength and viscous damping on the structure. In heave, configuration 5 and 6 have similar responses, where it seems to be slightly less response in configuration 6 around its resonance period compared to configuration 5. However they converge towards the same value of 1, except for ϵ=1/100 which tends to converge towards 1.5.

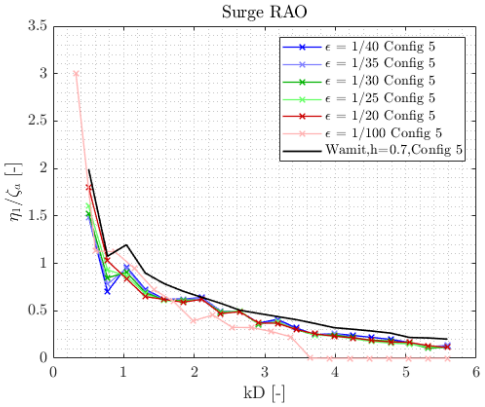

(a) Surge RAO Config 5

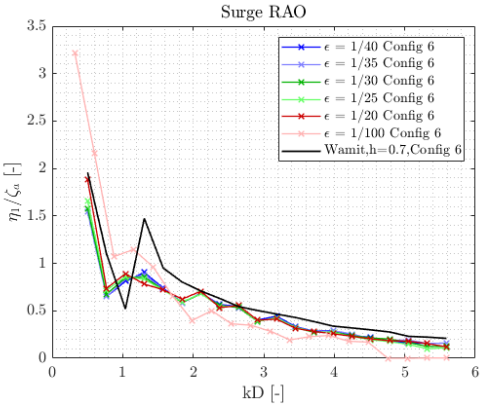

(b) Surge RAO Config 6

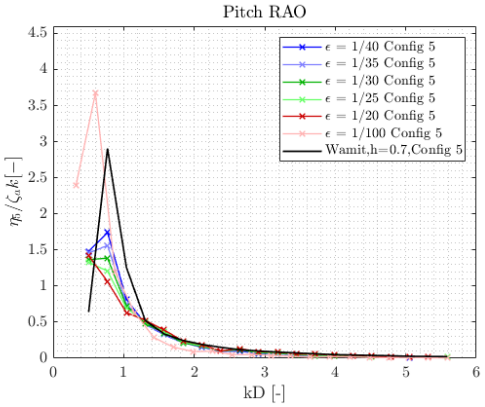

(c) Pitch RAO Config 5

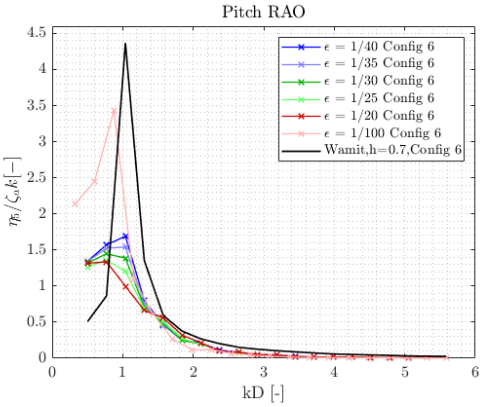

(d) Pitch RAO Config 6

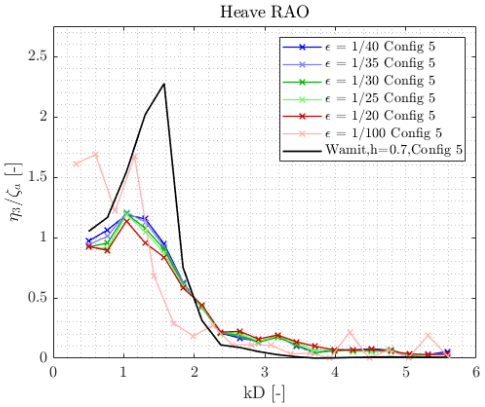

(e) Heave RAO Config 5

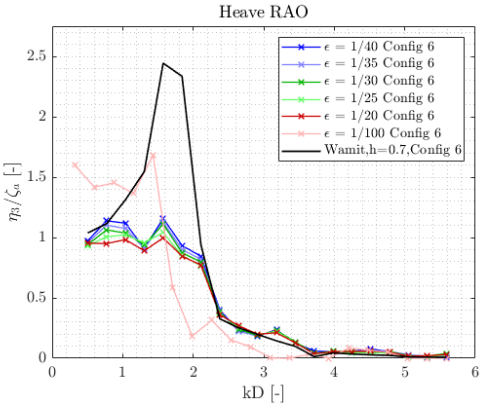

(f) Heave RAO Config 6

Figure 23: RAOs for configuration 5 and 6.

7.1.4 $\epsilon = 1/40$

In surge, configuration 3 stands out from the rest, by possessing lower responses than the other models for the given wave periods. This configuration also have the lowest response at resonance in pitch. Looking at the response in roll, found in Section C in the Appendix, configuration 3 have the highest response in roll. Given the shape of the RAOs in roll, this indicates non-linear movements, with uneven vortex shedding. Which might be due to a small perturbation from equilibrium, causing the motions

to increase with larger waves. With resonance in roll appearing at the same period which resonance occurs in pitch for all models, but also for the models with a large bilge keel in heave, this indicate there might be some Mathieu instability phenomenon occurring. However this needs to be checked further up on. There seems to be a trend in heave where models with the smaller bilge keel experience resonance at the same period, while the models with the larger keel experience resonance at a slightly higher period with a larger response. This suggests that at the given wave steepness, the difference in draught and pre-tension of mooring does not affect the response in heave. The bilge keel does, with its added mass and viscous damping functions. It is of interest to observe how the configurations with a smaller bilge experiences greater response in heave when the water depth turns from infinite to finite. Indicating that the response in heave might be affected by the water depth. At a kD period of 2, which equals to roughly 9 seconds, the response in configuration 2 are around 40 % larger than configuration 1. The difference are approximately equal for the other configurations.

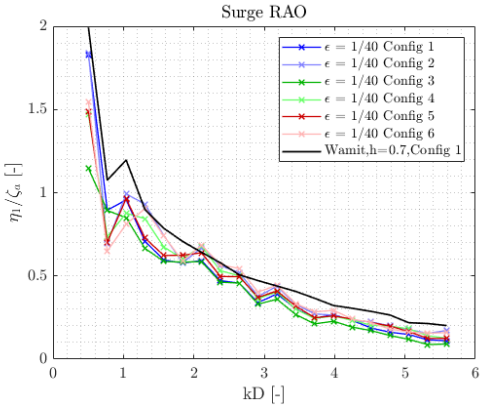

(a) Surge RAO all configurations

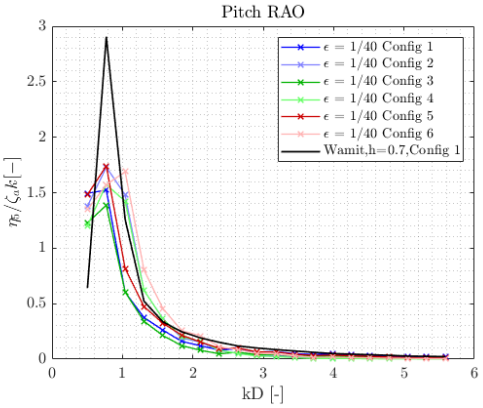

(b) Pitch RAO all configurations

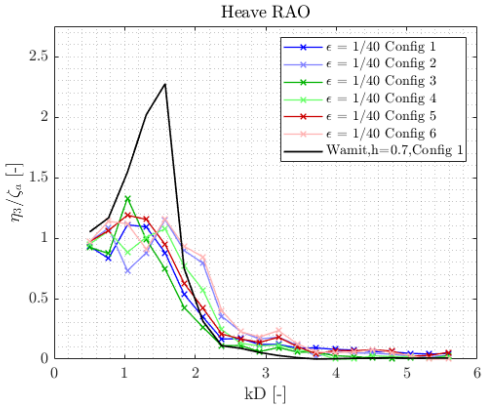

(c) Heave RAO all configurations

Figure 24: The RAOs for the different configurations at ϵ=1/40

The increase in heave around the period when the water depth turned from infinite to finite water depth due to the wave height, were also visible on the seabed in the wave tank due to dirt on the floor. Where there was sand formation around the model at smaller and shorter waves. Which provides an insight in how the viscous damping and added mass affected the sand on the seabed. At longer waves,

the model became more mass dominated, in combination with the movement of water particles in waves, causing the sand to drift behind the model in the tank. Configuration 1, at ϵ=1/40 was the first run in the wavetank, and therefore the only wave steepness it was possible to observe the sand on the seabed.

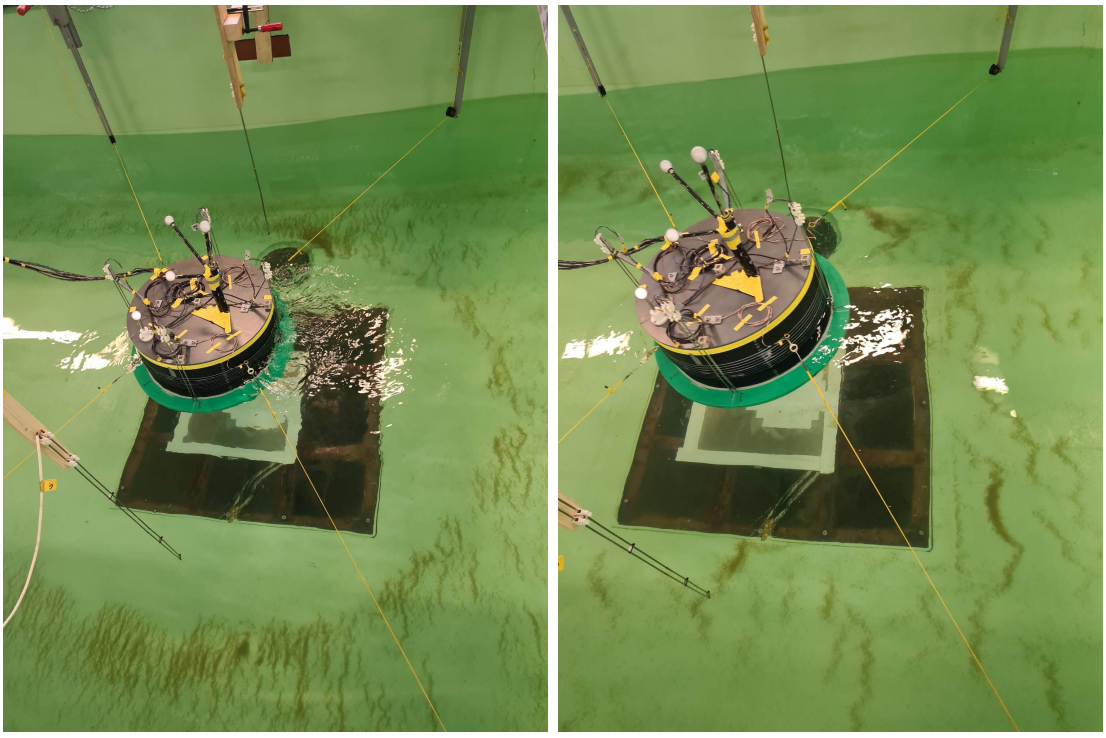

(a) Sand formation on seabed during waves in infinite water depth.

(b) Sand formation on seabed during waves in finite water depth.

Figure 25: Sand formation at ϵ=1/40

7.1.5 $\epsilon = 1/35$

The response in pitch starts to separate between the configurations, where it is observable that configuration 6 experience resonance at a slightly lower period than the other models. Which is likely due to the higher pre-tension on the mooring. In heave the trend at ϵ=1/40 continues at ϵ=1/35, where the response at resonance period is almost 1 for the models with small bilge keel. The response in roll is up to 50 % higher for configuration 3 compared to configuration 2 and 4. Where the trend currently indicates that the models with a smaller bilge keel are less exposed to roll motions.

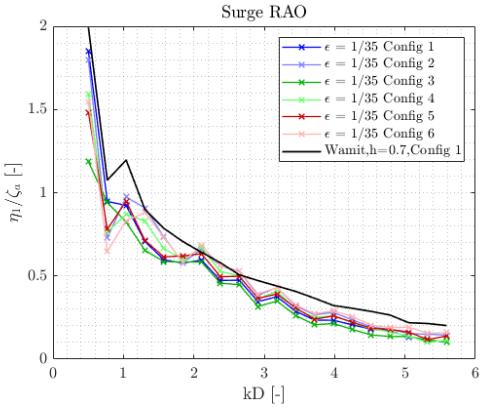

(a) Surge RAO all configurations

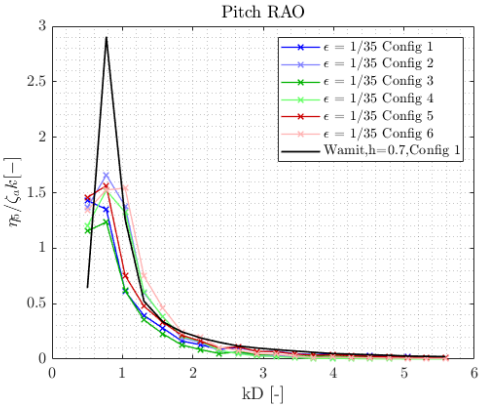

(b) Pitch RAO all configurations

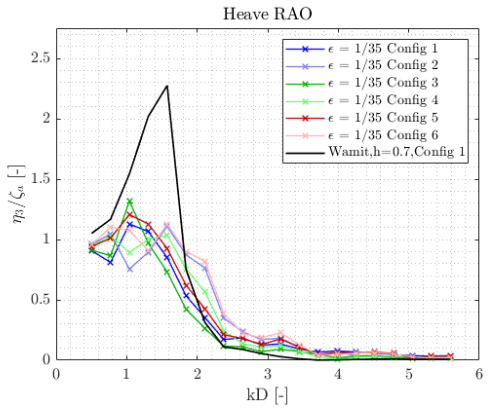

(c) Heave RAO all configurations

Figure 26: The RAOs for the different configurations at ϵ=1/35

7.1.6 $\epsilon = 1/30$

Configuration 3 experiences much larger responses on roll compared to the other models at this steepness. Whereas the responses in surge, pitch and heave did not change much at this wavelength compared to ϵ=1/35.

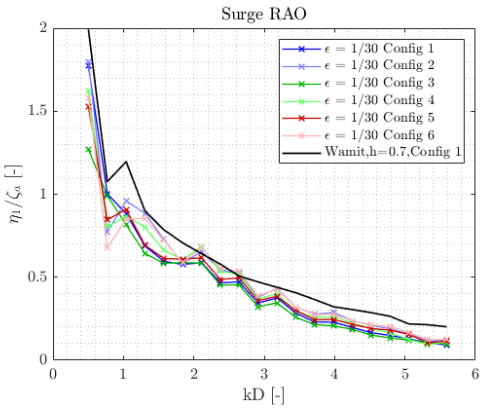

(a) Surge RAO all configurations

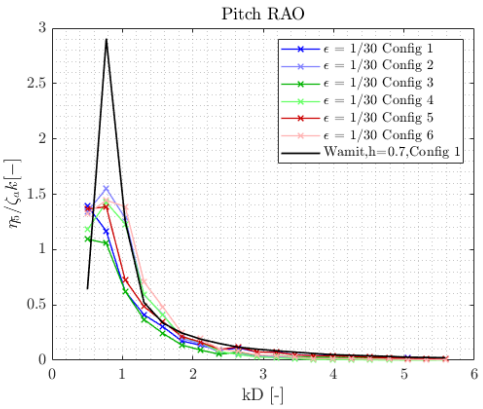

(b) Pitch RAO all configurations

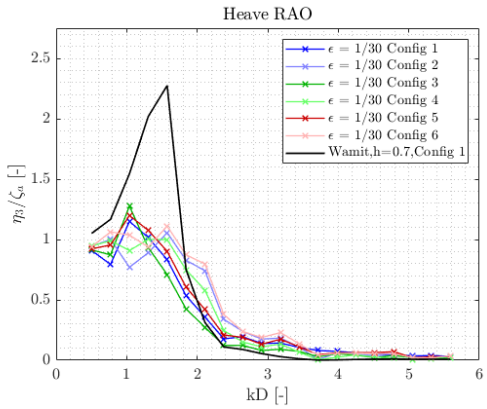

(c) Heave RAO all configurations

Figure 27: The RAOs for the different configurations at ϵ=1/30

7.1.7 $\epsilon = 1/25$

In surge, all the configurations responses are relatively similar. While in pitch it is observable that configuration 2,4 and 6, with the smaller keel, have a larger response when the period number is one. While configuration 3 has the lowest response in this motion. In heave the configurations with a large keel, 1, 3 and 5, experiences higher responses at their resonance period compared to the other models. While configuration 2, 4 and 6 converges to a RAO around 1 without any significant resonance period.

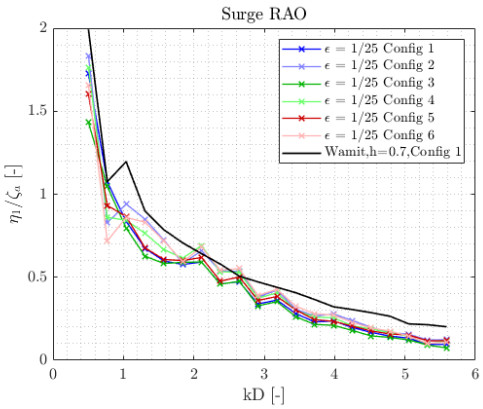

(a) Surge RAO all configurations

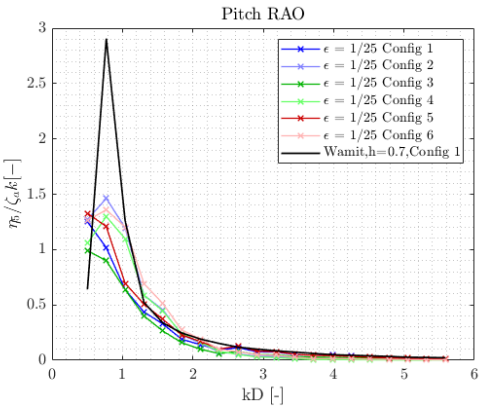

(b) Pitch RAO all configurations

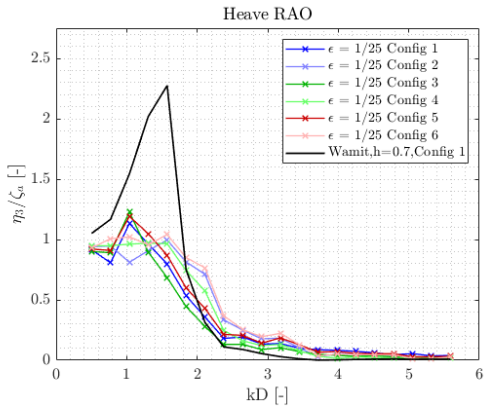

(c) Heave RAO all configurations

Figure 28: The RAOs for the different configurations at ϵ=1/25

7.1.8 $\epsilon = 1/20$

At such steep waves, there is almost no difference in the response in surge. However there are some differences in the response in pitch, where configuration 3 have the lowest overall responses. The differences in heave response reduces at steeper waves. There are differences between the models in roll, seen in Section C in the Appendix. With the lowest response in roll belonging to configuration 2 and 4.

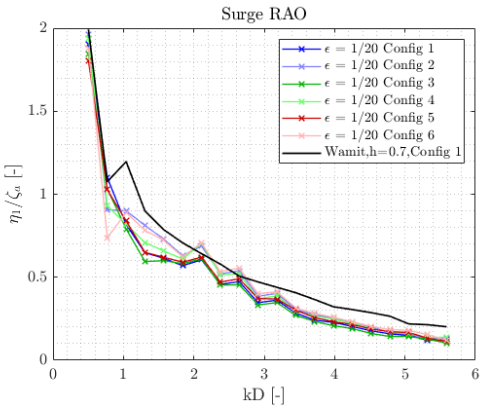

(a) Surge RAO all configurations

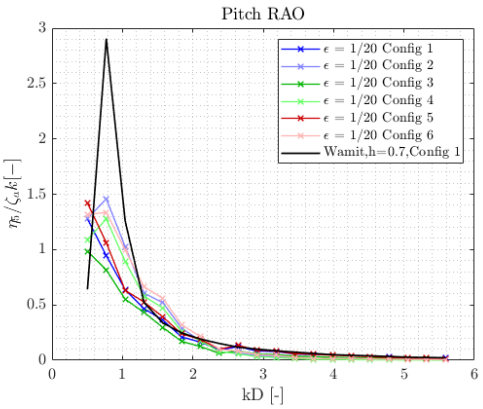

(b) Pitch RAO all configurations

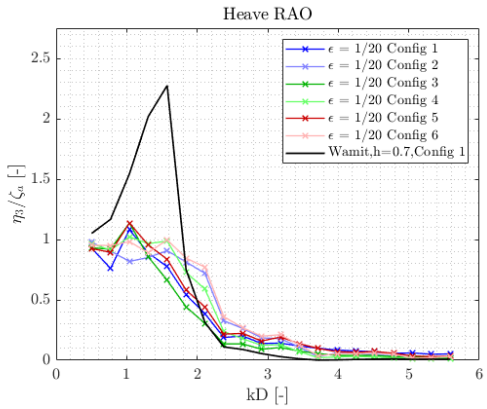

(c) Heave RAO all configurations

Figure 29: The RAOs for the different configurations at ϵ=1/20

At $\epsilon = 1/20$ there did occur some wave topping for all of the different configurations at the waves with a higher period/lower kD. However the amount of wave topping made it hard to interpret if it did affect the rigid body motions from the analyses. Some of the wave topping were caused by the viscous damping vortices "climbing up" and splashing water on the structure, as seen in Figure 30a. This causes wave overtopping, and have been called "vortice splash" under the picture. From the figure one can observe that this occurs after the wave peak has passed the structure, as the wave peak is at the end of the picture. The amount of water floating on deck after the event can be seen in Figure 30b. Which indicates that some of the water from the wave overtopping does not drain off before the next wave.

There are also provided some pictures in Figure 30c and 30d of the wave topping occurring for configuration 3. Which to a larger degree becomes almost submerged during the waves, due to the lower freeboard. Nevertheless, the quantity of water observed on deck, or measured from the wave probes on the model, was not significantly greater compared to the other configuration. From the relative wave elevation on the model figures in Figure 36 one can observe that there are not to much of a difference in relative wave elevation between the models. Which coincides with a relatively equal wave overtopping. Seen from the pictures there is a larger amount of water on deck, but it quickly drains off.

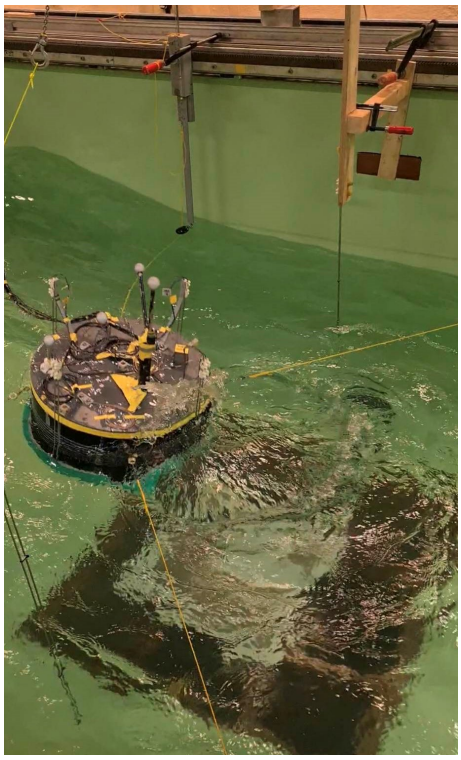

(a) Configuration 2 during "vortice splash"

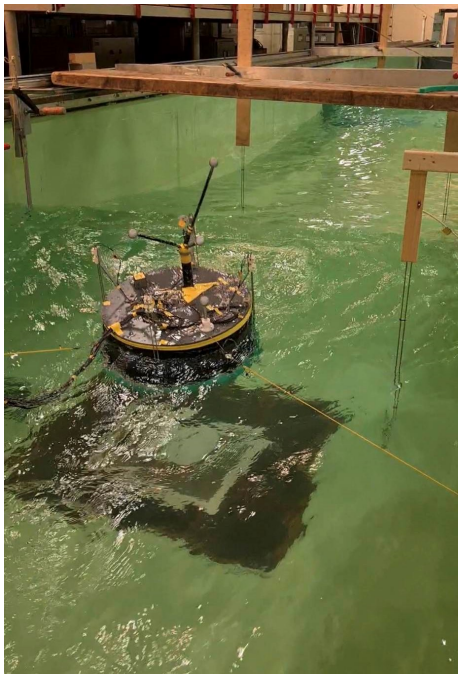

(b) Configuration 2 during wave overtopping

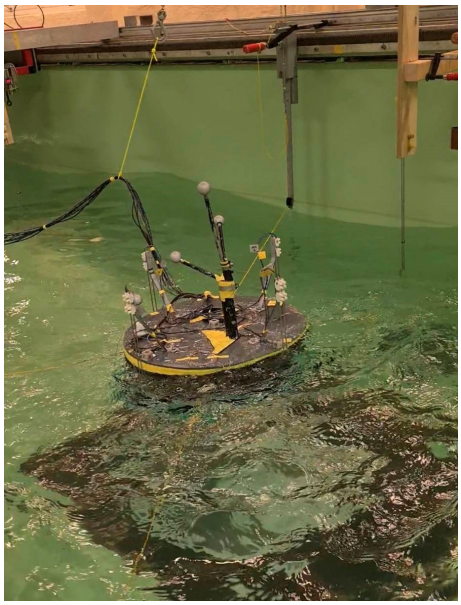

(c) Configuration 3 during wave overtopping

(d) Configuration 3 during wave overtopping

Figure 30: Pictures of wave overtopping occuring for two configurations.

7.1.9 $\epsilon = 1/100$

At $\epsilon = 1/100$ the responses in surge are relatively similar for all the configurations, except at the period of 1. At this point, configuration 2 and 4 experiences much lower responses than the others. This likely due to secondary order forces. In pitch the results are close to identical for the different configurations, and they seem to be converging in the area between 1.5 and 2.5. The maximum peak in pitch occurs at around the same period where configuration 2 and 4 experiences cancellation in surge. The numerical analysis are coincide with the experimental test, which indicates a high degree of linearity from the performed tests. In heave the results diverge to a larger extent. Where especially configuration 2 and 4 obtains lower responses compared to the other configurations. This might be due to cancellation of the Froude-Krylov force, and this occurs at around the same period where the secondary order forces occurs at in surge. At ϵ=1/100 the RAO in heave converge towards a value of 1.5, whereas it is lower for steeper waves. This is likely caused by more viscous damping at the steeper waves, due to less linearity. In roll there are hardly any response for any models at this steepness.

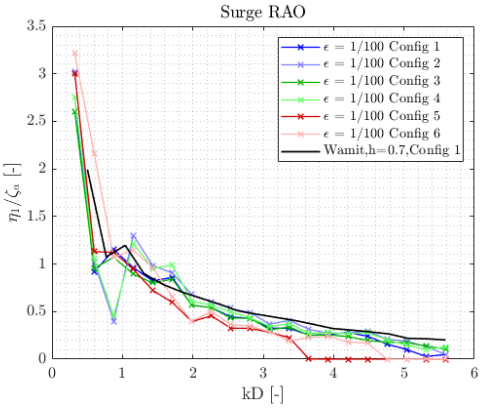

(a) Surge RAO all configurations

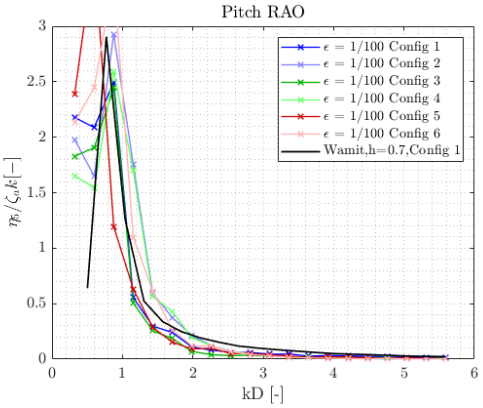

(b) Pitch RAO all configurations

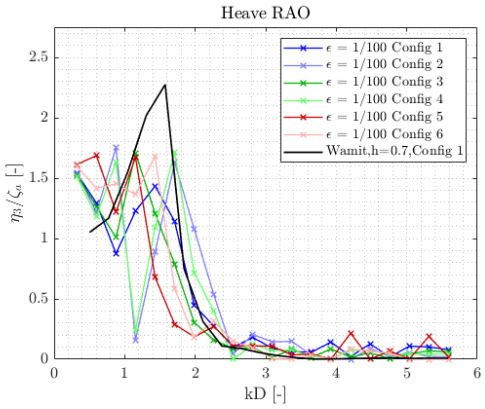

(c) Heave RAO all configurations

Figure 31: The RAOs for the different configurations at ϵ=1/100

8 Conclusion

In this thesis, a floating substation under development by Sevan SSP has been investigated. The concept revolves around the use of a circular cylindric hull, with a bilge keel, and a low freeboard. There have been conducted numerical analysis in Wamit and experiments in the Small Towing Tank (Lilletanken) at NTNU. The main goals was to examine how wave overtopping affected the rigid body motions in surge, heave and pitch, aswell as roll. However wave overtopping did not occur as frequent as supposed, changing the focus in the thesis to analyse how the different model configurations affects the rigid body motions. A total of six different configurations of the model have been tested, including a model-, draught- and mooring-study. In general the experimental and numerical results are seen as adequate in regards of validity from comparison. There are some discrepancies present due to viscous effects in the experiments that are not accounted for in the numerical simulations, as it assumes linear potential flow theory.

From the parameter study it became obvious that changes in the parameters did affect the numerical RAOs, however the changes was small. Which indicated that the changes in the bilge keel radius, draught, pre-tension of mooring or changes in I55 did not affect the response as much as assumed. However it provided useful insight in the motions of the structure.

The RAOs in surge for the experimental configurations do not differ much from each other, indicating that changes in bilge keel radius, draught or pre-tension does not affects the response to a large degree. In pitch however, there are more obvious differences between the models. Where especially configuration 3 obtains the lowest response in resonance. With configuration 1 and 4 also attaining good results as well. The RAOs in heave can be split into the configurations with large- and small-bilge keel. Where the models with a small keel do not seem to obtain a resonance period at steeper waves, while they also obtain cancellation of Froude Krylov force at less steep waves. Which provides configuration 2 and 4 with the most optimal results. By also considering the RAOs in roll, configuration 2 and 4 again have the better outcome. This provides us with a recommendation regarding which models that obtains the better results to be configuration 2 and 4. However this is very dependent on the wave spectra, and the location of its Tp values.

Another aspect which much be considered in regards of validity for the results are the scale the experiments have been performed at. At α=1/100, there are scaling effect differences between the model scale and full scale. In regards of viscous damping and added mass. In order to ensure a higher validity of the results, they should be compared to a scale model with larger dimensions.

9 Further work

The main focus in this thesis was an investigation of rigid body motions in different configurations. The following section includes proposals for further work on this thesis.

Due to a limited amount of time in the wavetank, because of delays, the number of configurations that was originally planned tested was not performed. Experiments for a configuration with a draught of 0.17 meter combined with higher pre-tension in the mooring are of interest. Another aspect which should be analysed in further work is to perform irregular wave tests on the different models, in order to examine the rigid body motions in irregular sea. As my hypothesis is that it will occur more frequent in irregular sea, making it possible to analyse how the wave overtopping affects the motions of the structure. Especially for the models with a low freeboard.

Another aspect which should be examined for further work is why the added mass and damping in the parameter study between configuration 2 and 6 are similar.

Bibliography

[1] Many Authors. *MARINE DYNAMICS*. Norwegian University of Science and Technology, Department of Marine Techonology, 2021.

[2] M. Ebbsesen and DNV. *Veikart for Havbruksnæringen*. 2017. URL: https://www.norskindustri.no/siteassets/dokumenter/rapporter-og-brosjyrer/veikart-havbruksnaringen_f41_web.pdf. (accessed: 06.12.2022).

[3] Odd Faltinsen. *Hydrodynamics of High-Speed Marine Vehicles*. Cambridge University Press, 2005.

[4] Odd Faltinsen. *Sea loads on ships and offshore structures*. Cambridge University Press, 1990.

[5] Inc. and Massachusetts Institute of Technology. *WAMIT User Manual Version 7.4*. WAMIT, Inc., 2020.

[6] Norsk Industri. *Floating Offshore Wind - Commercializing with Confidence*. URL: https://www.dnv.com/focus-areas/floating-offshore-wind/index.html. (accessed: 06.12.2022).

[7] Kwang-Leol Jeong and Young-Gill Lee. 'Numerical simulations of two-dimensional floating breakwaters in regular waves using fixed cartesian grid'. In: 6 (2014), pp. 206–218. DOI: https://doi.org/10.2478/IJNAOE-2013-0173.

[8] T. Koftis and P. Prinos. *Experimental study on wave overtopping of floating breakwaters*. 2006. URL: https://www.researchgate.net/publication/257251574_EXPERIMENTAL_STUDY_ON_WAVE_OVERTOPPING_OF_FLOATING-_BREAKWATERS. (accessed: 06.11.2022).

[9] S.W. Liao and R.W. Yeung. *Investigation of the Mathieu Instability of Roll Motion by a Time-Domain Viscous-Fluid Method*. 2001. URL: http://www.iwwwfb.org/Abstracts/iwwwfb16/iwwwfb16_25.pdf. (accessed: 12.10.2022).

[10] N/D. *Sevan Floating Substation Offshore wind and substation*. 2022. URL: https://sevanssp.com/floating-substation/. (accessed: 09.12.2022).

[11] N/D. *Sevan Floating Substation Offshore wind and substation*. 2023. URL: https://sevanssp.com/sevan-ccs/. (accessed: 01.06.2023).

[12] David Short. *Investigation into the Capabilities of Linear Theory for Numerical Modelling of Wave-Body Interactions for a 2D Heaving Buoy*. Master Thesis, NTNU, 2017.

[13] Qualisys Motion Capture Systen. *Motion Capture*. 2022. URL: https://www.qualisys.com/product-tag/oqus/. (accessed: 27.11.2022).

Appendix

A Measured wave heights

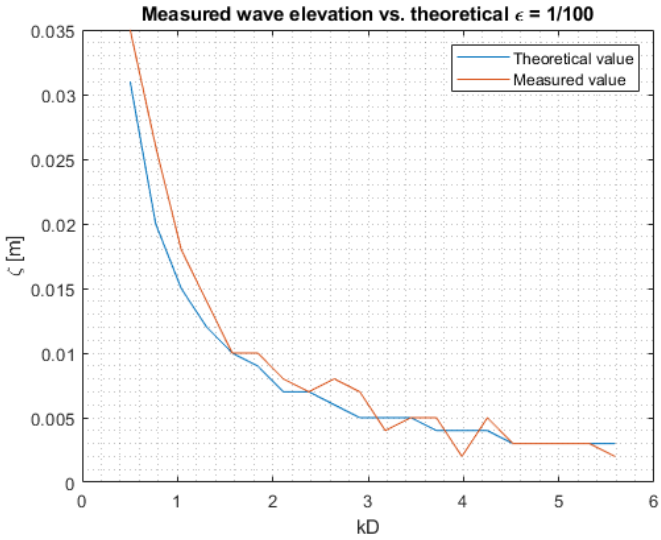

Figure 32: Measured waves at 100 steepness at WP 3 and 4

B Wamit Configurations

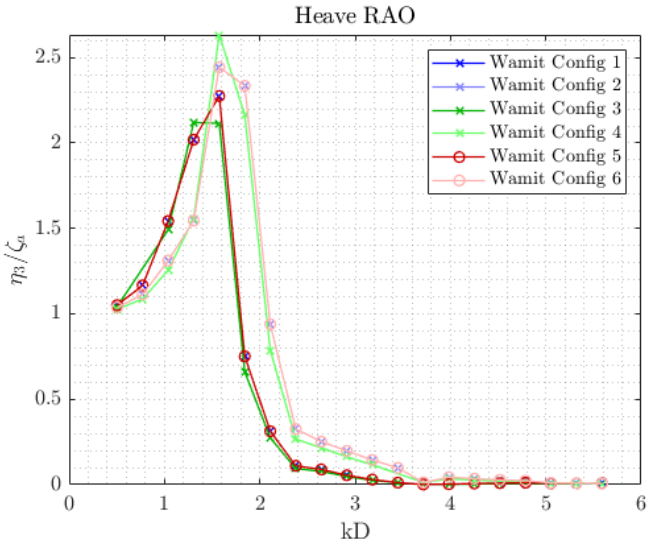

Figure 33: The different Wamit configurations

C Experimental RAOs in roll

C.1 Different steepness at same configuration

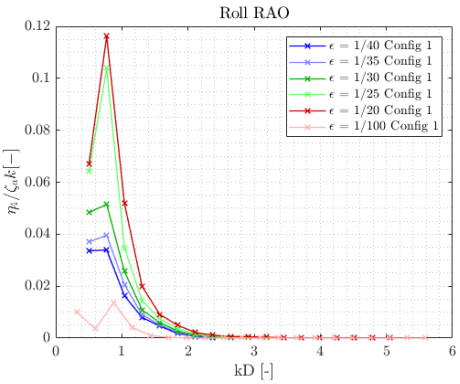

(a) Roll RAO Config 1 at different

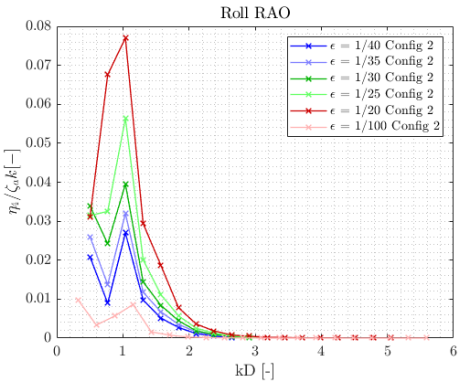

(b) Roll RAO Config 2

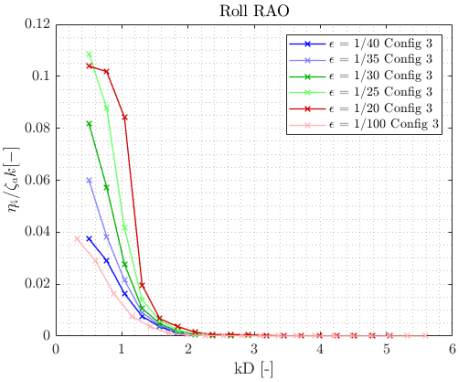

(c) Roll RAO Config 3

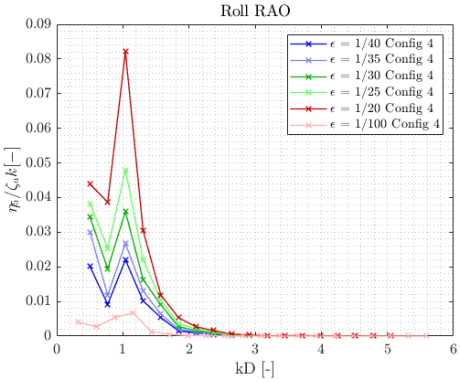

(d) Roll RAO Config 4

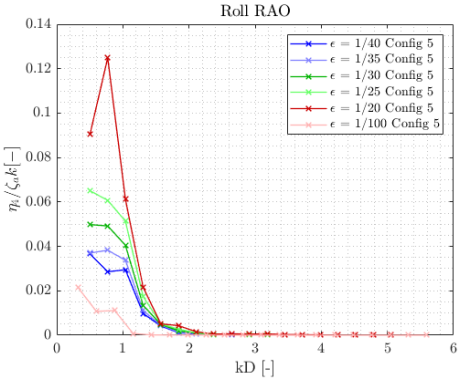

(e) Roll RAO Config 5

Figure 34: Experimental RAOs in roll for the different configurations

C.2 Different configurations at same steepness

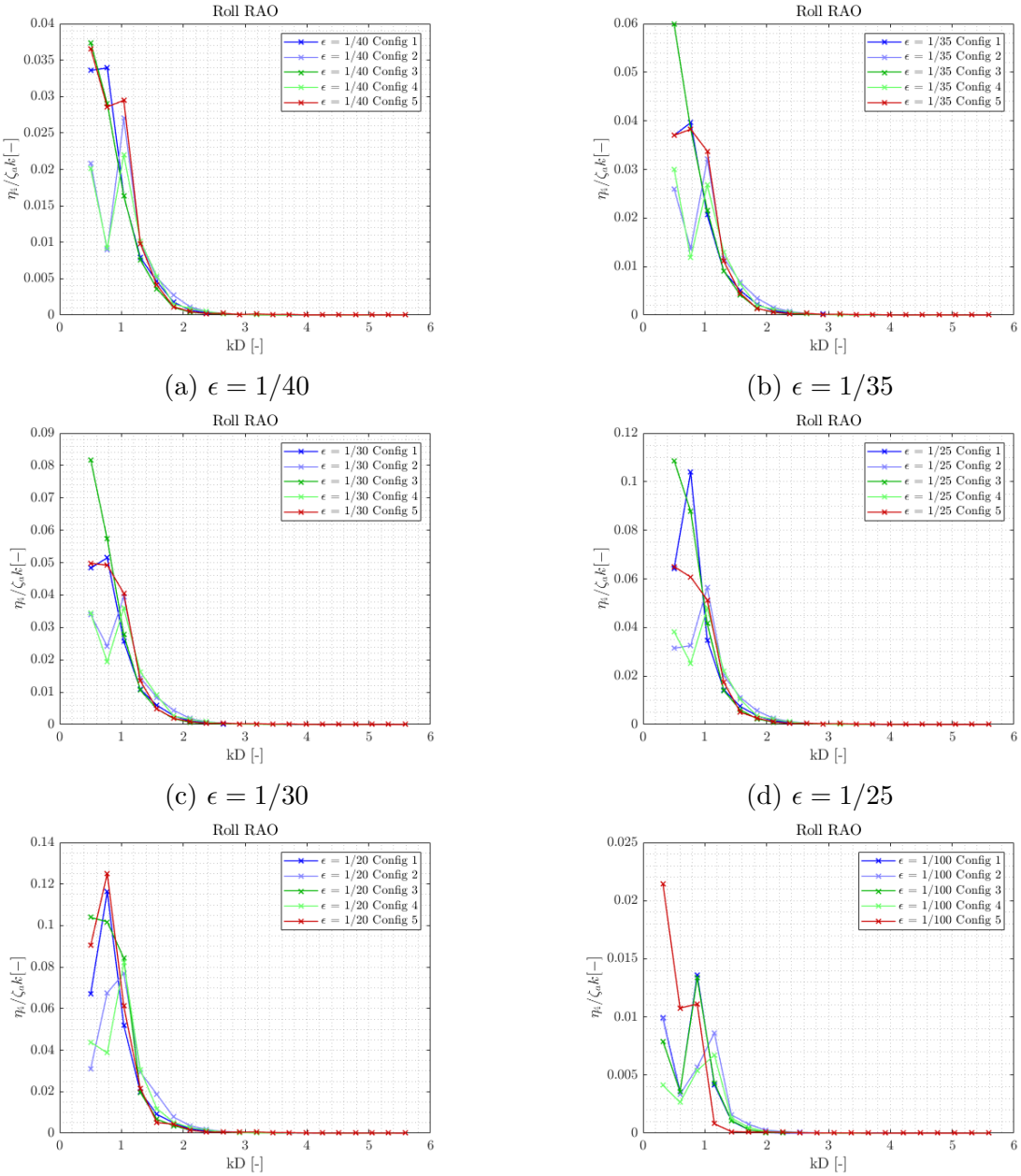

(a) $\epsilon = 1/40$

(b) $\epsilon = 1/35$

(c) $\epsilon = 1/30$

(d) $\epsilon = 1/25$

(e) $\epsilon = 1/20$

(f) $\epsilon = 1/100$

Figure 35: Experimental RAOs in roll for the different steepnesses

D Relative wave elevation on model

D.1 Different configurations

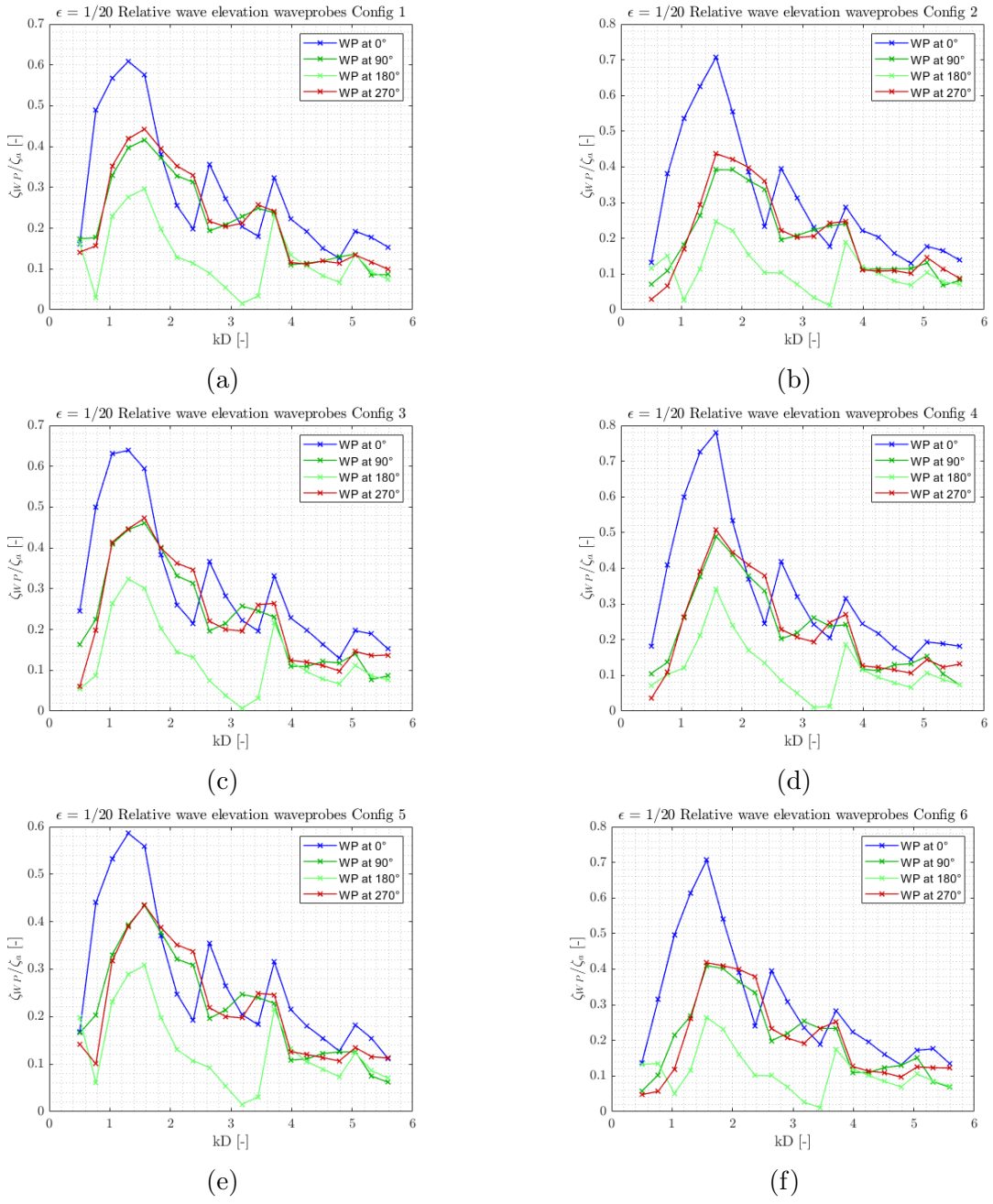

Figure 36: Relative wave elevation measured at model

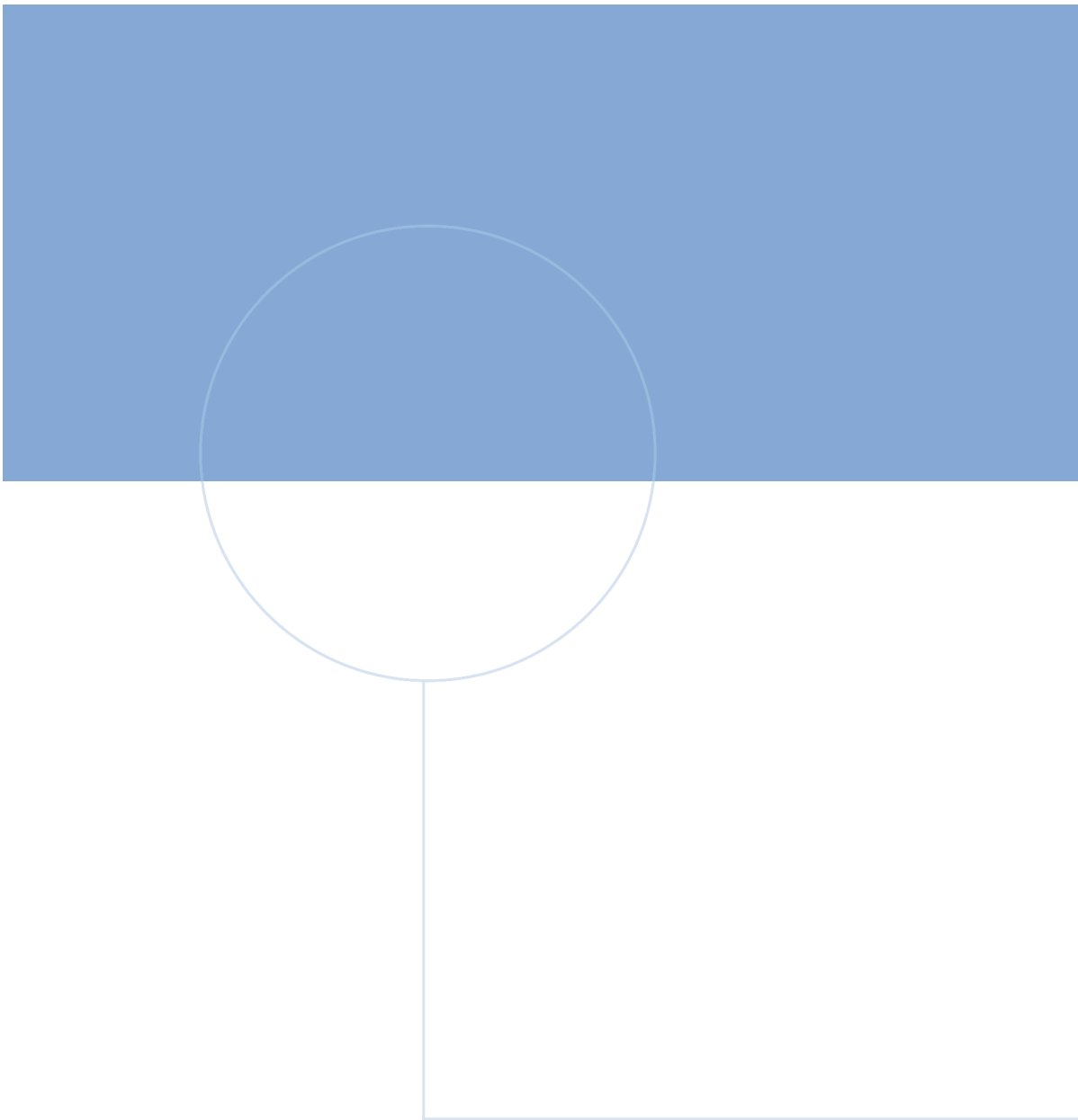

NTNU

Norwegian University of
Science and Technology